Universidade Federal do Rio Grande do Norte

Centro de Ciências Exatas e da Terra

Programa de Pós-Graduação em Geodinâmica e Geofísica

DISSERTAÇÃO DE MESTRADO

A DECONVOLUÇÃO DE EULER PODE DELINEAR CORPOS MAGNÉTICOS?

Autora:

Elizângela Soares Amaral Mota

Orientador:

Prof. Dr. Walter Eugênio de Medeiros (PPGG/UFRN)

Coorientador:

Dr. Roberto Gusmão de Oliveira (CPRM)

Dissertação nº 217/PPGG

Natal, RN, 23 de outubro de 2018.

UNIVERSIDADE FEDERAL DO RIO GRANDE DO NORTE

CENTRO DE CIÊNCIAS EXATAS E DA TERRA

PROGRAMA DE PÓS-GRADUAÇÃO EM GEODINÂMICA E GEOFÍSICA

DISSERTAÇÃO DE MESTRADO

A DECONVOLUÇÃO DE EULER PODE DELINEAR GEOMETRIA DE CORPOS MAGNÉTICOS?

Autora:

Elizângela Soares Amaral Mota

Dissertação apresentada em 23 de outubro de 2018, ao Programa de Pós-Graduação em Geodinâmica e Geofísica-PPGG, da Universidade Federal do Rio Grande do Norte – UFRN como requisito à obtenção do Título de Mestre em Geodinâmica e Geofísica, com área de concentração em Geofísica.

Comissão Examinadora

Prof. Dr. Walter Eugênio de Medeiros (PPGG/UFRN – Orientador)

Profa. Dra. Roberta Mary Vidotti (IG/UNB) - Examinadora externa

Prof. Dr. David Lopes de Castro (PPGG/UFRN) - Examinador interno

Natal, RN, 23 de outubro de 2018.

Resumo

Pesquisas metodológicas apontaram sérias limitações da deconvolução de Euler (ED) para delinear a forma da fonte. No entanto, a ED tem sido extensivamente empregada em dados de campo para delinear interfaces e estimar mergulhos de falhas e zonas de cisalhamento, evidenciando uma divergência entre os resultados teóricos e práticos desta técnica. Para conciliar essa discordância, mostramos que o ED pode ajudar a inferir informações úteis sobre o volume e o mergulho da fonte, quando aplicado às anomalias reduzidas ao polo causadas por dois tipos de corpos. No primeiro, o corpo pode ter contraste uniforme de magnetização, mas interfaces rugosas. O mergulho pode então ser estimado grosseiramente a partir do agrupamento das soluções. No segundo tipo, as interfaces do corpo podem ser lisas, mas apresentarem contrastes internos de magnetização. Neste caso, além de mergulho, pode-se delimitar aproximadamente o volume da fonte a partir do envelope do agrupamento de soluções. Para corroborar os resultados teóricos, a ED foi aplicada em duas anomalias aeromagnéticas: uma delas associada com uma zona de empurrão e a outra com um corpo de formação ferrífera bandada. Estes dois casos foram escolhidos como exemplos reais dos experimentos teóricos: para a zona de empurrão, o agrupamento de soluções segue sua forma geológica conhecida e permite estimar a variação do mergulho, enquanto que para a formação ferrífera bandada, o agrupamento de soluções se espalha ocupando um volume. Para o último caso, uma modelagem direta 3D sobre a anomalia real também foi realizada para estimar a distribuição de magnetização e a ED foi aplicada para o ajuste da anomalia sintética. O agrupamento de soluções resultante é semelhante ao obtido com a anomalia de campo, mostrando a consistência dos resultados de ED. A partir dos resultados obtidos, pode-se concluir que a ED realmente não delineia a forma da fonte, mas que informações úteis sobre mergulho e volume podem, de fato, ser inferidas.

Palavras-chaves: Magnetometria; deconvolução de Euler; modelagem magnética.

Abstract

Methodological researches have pointed out severe limitations of Euler deconvolution (ED) to outline source shape. However ED has been extensively employed on field data to outline interfaces and estimate dips of faults and shear zones, evidencing a disagreement between theoretical and practical results of the tool. To reconcile this disagreement, we show that ED might help to infer useful information about source volume and dip, when it is applied to the reduced-to-the-pole anomalies caused by two types of body. In the first, the body might have uniform magnetization contrast but rough interfaces. The dip can then be grossly estimated from the solution cluster. In the second type, the body interfaces might be smooth but it has internal magnetization contrasts. Now, besides dip, one can delimit approximately the source volume from the solution cluster envelope. ED was also applied to field anomalies, which are caused by a curved-shape thrust zone and by a banded iron formation. These two field cases were considered as examples of anomalies caused by the described first and second types of bodies, being the ED results similar for each body type: for the thrust zone, the solution cluster follows its known geologic shape and allows to estimate dip variation whilst, for the banded iron formation, the solution cluster spreads out occupying a volume. For the latter case, a forward 3D modeling of the field anomaly was also performed to estimate the magnetization distribution and ED was applied to the fit synthetic anomaly. The resulting solution cluster is similar to the one obtained with the field anomaly, showing the consistency of the ED results. From the obtained results, it can be conclude that ED does not really outlines source shape but that useful information about dip and volume might be indeed inferred.

Keywords: Magnetometry; Euler deconvolution; magnetic modeling.

Agradecimentos

Agradeço primeiramente a Deus pelo dom da vida e por todo ensinamento.

Agradeço a meus pais pela dedicação, amor e carinho que sempre tiveram por mim e por todos os exemplos de amor ao próximo que me ensinarem ao longo da vida.

Agradeço a meu esposo Assis pela compreensão e palavras de incentivo que foram fundamentais desde o início para que esse sonho fosse realizado.

Agradeço ao meu orientador prof. Dr. Walter Eugênio de Medeiros pela orientação, paciência e dedicação durante esta jornada.

Agradeço ao meu grande amigo e coorientador Roberto Gusmão de Oliveira que é um dos meus maiores incentivadores desde que ingressei na CPRM. Ele é um dos responsáveis para que essa conquista fosse alcançada.

Agradeço a CPRM pela concessão da licença para eu cursar a pós-graduação, além do apoio em ceder os dados aerogeofísicos e de cartografia geológica possibilitando a conclusão deste trabalho.

A todos os meus amigos e colegas de trabalho da CPRM de Teresina e de outras unidades que torceram e me ajudaram para a realização desse trabalho. Em especial a Joseneusa, Vladimir, Valdir, Rubens, Ciro, José Alberto, Nilo, Magno, Evilarde, Douglas, Camila, Magno, Reginaldo, Ricardo, Paula, Tereza.

Agradeço aos meus companheiros de pós-graduação, Alex, Renato, Márcio, Nitzchia, Jeberson, Rafaela, Alanny, Gilsijane, pelas trocas de experiências essenciais em todas as etapas desse projeto.

_____

Sumário

_____

Capítulo 1

Introdução e Objetivos

1.1 Elementos do campo geomagnético

O vetor do campo magnético total possui três componentes ortogonais nas direções X, Y e Z (Figura 1). A declinação magnética é o ângulo entre o norte geográfico e o norte magnético e a inclinação I refere-se ao ângulo entre o vetor campo total H e o plano horizontal. A inclinação do campo magnético varia de acordo com a latitude magnética. Isso implica que um corpo com mesma intensidade de magnetização pode ter variação na forma e amplitude da anomalia magnética dependendo da latitude da Terra em que o corpo estiver localizado.
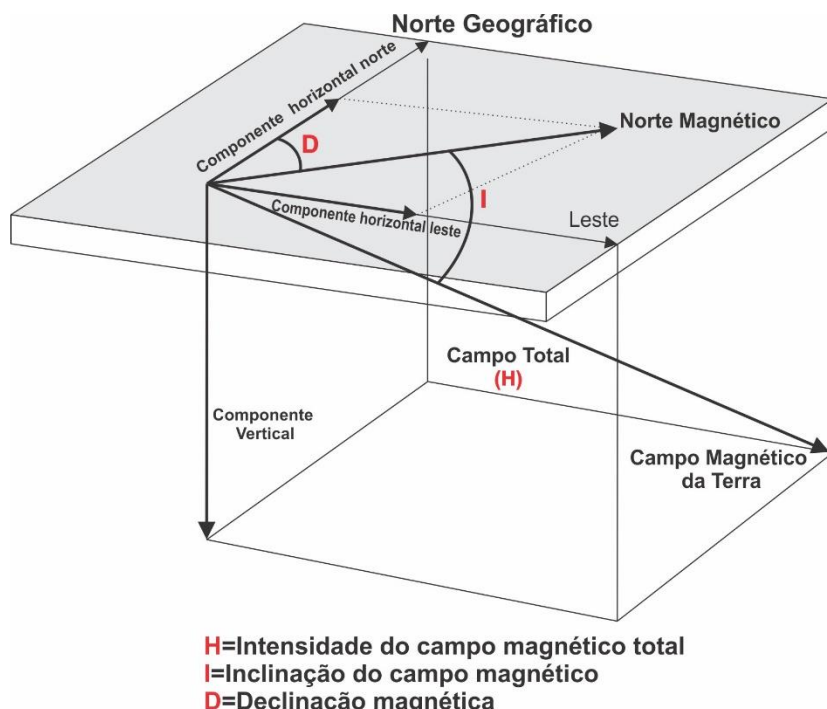

Figura 1: Representação gráfica dos elementos do campo geomagnético (modificado de Kearey et al., 2002).

1.2 Justificativa e Objetivos

Para atender a necessidade de interpretar grande volume de dados aeromagnéticos de forma rápida, a partir da década de 70 surgiram os métodos automáticos (Barbosa e Silva, 2005), por exemplo: deconvolução de Werner (Hartman et al., 1971); o método de Naudy (Naudy, 1971); o método de CompuDepth (O'Brien, 1972); e a deconvolução de Euler (ED) (Thompson, 1982). Dentre eles, o mais popular é o método de Thompson (1982) desenvolvido para estimar simultaneamente a posição e tipo de fontes magnéticas. Devido a isto, o método tem sido discutido e aperfeiçoado por diversos autores (Barbosa et al., 1999; Barbosa et al., 2000; Silva et al., 2001; Reid 2003; Cooper, 2004; FitzGerald et al. 2004; Mushayandebvu 2004; Melo et al. 2013; M. Fedi, 2013; Guoqing Ma, 2014; Melo e Barbosa 2017, entre outros) e atualmente é uma das técnicas mais utilizadas para interpretação prática de dados potenciais. No entanto, estudos analíticos destacam algumas deficiências da ED (Barbosa & Silva, 2005), dentre elas: a) presença de nuvem de soluções espúrias obtidas pelo critério de Thompson (1982); b) necessidade de conhecimento a priori do índice estrutural (IE); c) limitações na determinação de susceptibilidade; d) dificuldade em inferir mergulho de fontes magnéticas e e) ineficácia para determinar a forma tridimensional de fontes anômalas (Uieda et al., 2014).

Apesar das limitações apontadas por pesquisas metodológicas, a ED vem sendo largamente utilizada na prática em diversas áreas para interpretação de dados potenciais, por exemplo: detectar lineamentos, falhas, *trends* e/ou contatos geológicos (Ferracioli et al., 2002; Oruç and Keskinsezer, 2008; Reeh et al., 2008; El-Gout et al., 2010; Oruç and Selim, 2011; Araffa et al., 2012; Gohl et al., 2013; Al-Saud. 2014; Rocha et al., 2014; Araffa et al., 2015; Hadhemi et al., 2016; Wang et al., 2017; Martins-Ferreira et al., 2018; Weiherman et al., 2018), localizar zonas de sutura (Bournas et al., 2003), estimar parâmetros de falhas (Ndougsa-Mbarga et al., 2012; Chen et al., 2014; Harrouchi et al., 2016; Khalil et al., 2016; Awoyemi et al., 2017; Bahrudin and Hamzah, 2018), localizar falhas para fazer correlações com hipocentros no caso de estruturas sismogênicas (Mazabraud et al., 2005; Minelli et al., 2016), delinear estruturas e/ou blocos tectônicos em bacias sedimentares (Anand et al., 2009; Chandrasekhar et al., 2009; Ferraciolli et al., 2009; Castro, 2011; Cooper et al., 2011; Castro et al., 2014; Dhaoui et al., 2014; Curto et al., 2015; Sridhar et al., 2017), delinear estruturas de impacto (Werner et al., 2010), caracterizar zonas ou corpos de ferro (Mieth et al., 2014; Alamdar et al., 2015; Alamdar,

2016; Oladunjoye et al, 2016; Moghtaderi et al., 2017; Olasunkami et al., 2017),localizar corpos anômalos crustais (Ebbing et al., 2007; Alrefaee et al., 2017), e mapear estruturas do embasamento em áreas Precambrianas (Osinowo et al., 2014; Zhang et al., 2015; Akinlalu et al., 2018; Ibraheem et al., 2018).

Portanto, existe uma lacuna entre os estudos metodológicos e a comunidade científica que utiliza a ED na prática que precisa ser melhor entendida: se pesquisas metodológicas apontam que as soluções da ED estão associadas apenas ao topo das fontes ou estimam no máximo uma localização aproximada da fonte, qual o significado geológico das soluções obtidas nas aplicações práticas que não estão correlacionadas com o topo das fontes anômalas? O objetivo desse trabalho foi demonstrar que os modelos sintéticos precisam reproduzir melhor corpos geológicos reais para diminuir as discrepâncias entre as duas abordagens.

Capítulo 2

Materiais e Métodos

A metodologia aplicada obedeceu quatro passos: a) modelagem direta magnética 3D para corpos sintéticos; b) transformação de redução ao polo; c) aplicação da deconvolução de Euler no ambiente do *Oasis Montaj*; d) filtragem de soluções espúrias.

3.1 Modelagem Direta 3D para corpos sintéticos

A modelagem magnética direta foi feita usando a abordagem de Okabe (1979). Baseado no princípio da superposição e o teorema de Poisson associado à terceira identidade de Green, Okabe (1979) deduziu uma expressão analítica para calcular o campo magnético produzido por um corpo poliédrico com facetas poligonais e magnetização uniforme (ver apêndice).

2.2 O Filtro Redução ao Polo Magnético

A forma da anomalia magnética depende tanto da geometria da fonte quanto das direções vetoriais de magnetização. Com exceção dos polos e equador magnético, as anomalias magnéticas apresentam caráter dipolar, o que dificulta sua interpretação. Sendo assim, para interpretar dados magnetométricos em regiões de latitudes magnéticas baixas ou intermediárias é comum utilizar a transformação de redução ao polo, permitindo centralizar o pico positivo sobre a fonte anômala (Figura 2), (Silva, 1986; Blakely, 1995). Este tipo de filtragem torna a direção de mergulho dos corpos mais evidente. Além disso, a deconvolução de Euler aplicada no campo magnético reduzido ao polo produz estimativas de profundidades mais precisas (Thompson, 1982).
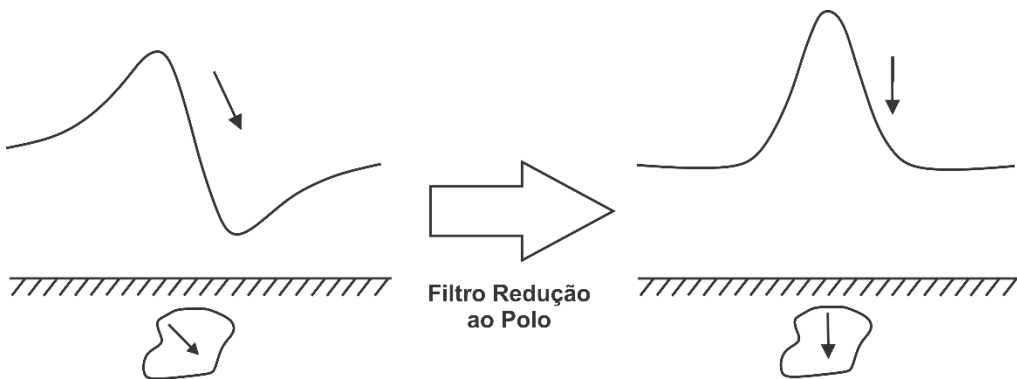
Figura 2: Esquema da aplicação do filtro de redução ao polo (Blakely, 1996).

No entanto, este tipo de filtragem pode introduzir alinhamentos espúrios na direção da declinação magnética quando aplicado em anomalias localizadas em baixa latitude magnética (Blakely, 1996). Para diminuir o exagero das feições N-S causadas como efeito desse filtro foi empregada uma pseudo-inclinação que consiste em aplicar correção na componente de magnitude do algoritmo (Geosoft, 2015).

No domínio da frequência, o operador matemático da redução ao polo magnético é definido pela expressão:

$$L(\theta) = \frac{1}{[sen(I) - i\cos(I)*\cos(D-\theta)^2]} \qquad \text{Eq. (2.1)}$$

onde I=inclinação magnética; D=declinação magnética e θ é o número de onda. À medida que I se aproxima de zero e (D-θ) se aproxima $\pi/2$, o operador se aproxima do infinito e a equação se torna instável, o que ocorre frequentemente em regiões de baixas a intermediárias latitudes magnéticas. Sendo assim, a instabilidade pode ser minimizada pelo uso da pseudo-inclinação (Ia) que é usada para controlar a amplitude do uso do filtro:

$$L(\theta) = \frac{1}{[sen(I_a) - i\cos(I)*\cos(D-\theta)^2]} \qquad \text{Eq. (2.2)}$$

Geralmente, utilizamos empiricamente o valor do complemento da inclinação para este fator de correção.

2.3   O Problema Inverso: Deconvolução de Euler 3D

O método de Thompson (1982) é uma técnica de modelagem geofísica inversa baseada na equação da homogeneidade de Euler:

$$(x - x_0)\frac{\partial T}{\partial x} + (y - y_0)\frac{\partial T}{\partial y} + (z - z_0)\frac{\partial T}{\partial z} = -\eta T ,$$ Eq.(2.3)

em que (x_0, y_0, z_0) representa a posição da fonte magnética cujo campo total T é detectado em (x,y,z). O grau de homogeneidade η está associado com um índice estrutural, que é a medida da taxa de decaimento do campo magnético em função da distância de sua fonte e varia de acordo com a fonte magnética. O processo inverso relaciona o campo magnético e os componentes do gradiente para a localização das fontes de uma anomalia, com base no índice estrutural ($\eta = 0$ para contato, $\eta = 1$ para dique, $\eta = 2$ para cilindro e $\eta = 3$ para esfera).

Como tentativa de simular uma aproximação local para obter uma separação regional-residual, assume-se uma perturbação no campo magnético tal que: $h \equiv h\ (x, y, z) = T(x, y, z) + b$, admitindo-se informação preliminar do índice estrutural e sendo b um nível de base desconhecido. Desta forma, a Equação (2.3) torna-se:

$$x_0\frac{\partial h}{\partial x} + y_0\frac{\partial h}{\partial y} + z_0\frac{\partial h}{\partial z} + \eta b = x\frac{\partial h}{\partial x} + y\frac{\partial h}{\partial y} + z\frac{\partial h}{\partial z} + \eta h$$ Eq.(2.4)

A equação (2.4) pode ser escrita na forma matricial:

$$\begin{pmatrix} \frac{\partial h_1}{\partial x} & \frac{\partial h_1}{\partial y} & \frac{\partial h_1}{\partial z} & \eta \\ \vdots & \vdots & \vdots & \vdots \\ \frac{\partial h_N}{\partial x} & \frac{\partial h_N}{\partial y} & \frac{\partial h_N}{\partial z} & \eta \end{pmatrix} \bullet \begin{pmatrix} x_0 \\ y_0 \\ z_0 \\ b \end{pmatrix} = \begin{pmatrix} x_1\frac{\partial h_1}{\partial x} + y_1\frac{\partial h_1}{\partial y} + z_1\frac{\partial h_1}{\partial z} + \eta h_1 \\ \vdots \\ x_N\frac{\partial h_1}{\partial x} + y_N\frac{\partial h_1}{\partial y} + z_N\frac{\partial h_1}{\partial z} + \eta h_N \end{pmatrix}$$ Eq. (2.5)

A equação (1.3) representa um problema inverso linear da forma $\boldsymbol{G\,m = d}$, onde a matriz $\boldsymbol{G} \in R^{(N \times 4)}$ é o operador linear, $\boldsymbol{m}$ representa o vetor de parâmetros do modelo e **d** o vetor das observações.

Admitindo-se um valor conhecido para o índice estrutural, a metodologia de Euler estima as coordenadas da fonte anômala (x_0, y_0 e z_0), e o nível de base (b). Esses parâmetros são calculados dentro de um intervalo, conhecido como janela móvel de dados, aplicando-se o método dos quadrados mínimos na equação (2.5):

$$\hat{m} = (\boldsymbol{G}^T\boldsymbol{G})^{-1}(\boldsymbol{G}^T\boldsymbol{d}) \, , \qquad\qquad \text{Eq.(2.6)}$$

sendo $\hat{m} = (\hat{x}_0 \ \hat{y}_0 \ \hat{z}_0 \ \hat{b})^T$ o vetor das estimativas dos parâmetros.

2.4   Critérios de Filtragem

Utilizamos dois critérios de filtragem: a) tolerância máxima nas incertezas de profundidade; b) critério do volume de filtragem.

2.4.1   Tolerância máxima das incertezas nas estimativas de profundidade

Segundo Thompson (1982), o critério de aceitação das soluções deve atender:

$$\frac{\hat{z}_0}{\eta \sigma_{\hat{z}_0}} > \varepsilon \qquad\qquad \text{Eq.(2.7)}$$

$\sigma_{\hat{z}_0}$ é o desvio padrão de $\hat{z}_0$ e ε um escalar positivo fornecido pelo intérprete. O desvio padrão é tratado como uma "barra de erro" na estimativa de profundidade e forma a base para um algoritmo que determina se uma estimativa de profundidade deve ou não ser aceita. Cada estimativa aceita e relacionada com uma dada janela de dados é considerada como uma possível solução e um símbolo (representando o índice estrutural presumido) é plotado nas coordenadas (x_0, y_0, z_0). O índice estrutural experimental que produz a menor dispersão das soluções é selecionado como a melhor estimativa do verdadeiro (Thompson, 1982). O critério deve aceitar a estimativa de η que produza a menor dispersão das soluções.

Utilizamos o critério proposto por Reid et al. (1990). Os autores recomendam aceitar as soluções associadas a incertezas nas estimativas de profundidade limitadas em até 15%.

2.4.2   Volume de Filtragem

O segundo critério adotado é aplicado após a filtragem pelas incertezas das profundidades. É um critério empírico simples que desenvolvemos e consiste em descartar as soluções que estão localizadas fora de um dado prisma oblíquo definido por oito vértices (Figura 3). As faces superior e inferior do prisma são paralelas à superfície da Terra e podem ser retângulos ou losangos. As dimensões e mergulho do prisma (ângulo α na figura) são inferidas a partir da análise visual do conjunto de soluções ED e da anomalia reduzida a polo, de modo que, de acordo com a avaliação do intérprete, o prisma contém as soluções aceitáveis. Em particular, as dimensões horizontais do prisma devem ser grandes o suficiente para conter o conjunto de soluções mais rasas que delineiam a face superior da fonte magnética.
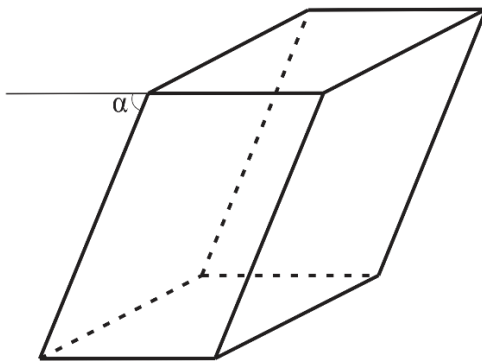

Figura 3: Exemplo do prisma – segundo critério de filtragem

Por geometria analítica, criamos um algoritmo de forma que inicialmente obteve-se o vetor unitário normal a cada face. Depois, para cada solução foi calculado o produto escalar do vetor distância entre essa estimativa e a normal a cada face ($\hat{\boldsymbol{n}}_k$). Se o resultado dessa operação fosse maior ou igual à zero para todas as faces, a solução seria aceita. Se ao menos um produto escalar fosse negativo, a solução seria considerada espúria e eliminada do conjunto original de profundidades estimadas.

2.5 Aplicações

Para verificar a eficácia da metodologia, inicialmente, fizemos testes em corpos sintéticos de formas que os mesmos representassem o máximo possível, corpos geológicos reais.

A área de estudo para aplicação real da metodologia está localizada no Estado do Piauí, nordeste do Brasil na região sudoeste da Província Borborema e noroeste do Cráton São Francisco (Figura 4). Grande parte dos corpos e estruturas associadas às fontes magnéticas não aflora. Portanto, supõe-se que a sua continuidade em subsuperfície pode ser melhor caracterizada aplicando-se o método de deconvolução de Euler. Além disso, as duas áreas foram sistematicamente escolhidas de forma que cada uma represente os principais resultados obtidos nos dados sintéticos. A primeira, localizada na Faixa Riacho do Pontal está associado à uma zona de empurrão sendo que a anomalia magnética pode estar correlacionada ao dado sintético que reproduz material magnético fino colocado em ambiente compressivo. O segundo corpo, localizado na porção noroeste do Cráton São Francisco corresponde a uma sequência meta-vulcano-sedimentar com formações ferríferas bandadas, que possuem zonas contendo concentrações massivas de minério de ferro. A anomalia pode ser comparada ao resultado do dado sintético com contraste interno de magnetização.
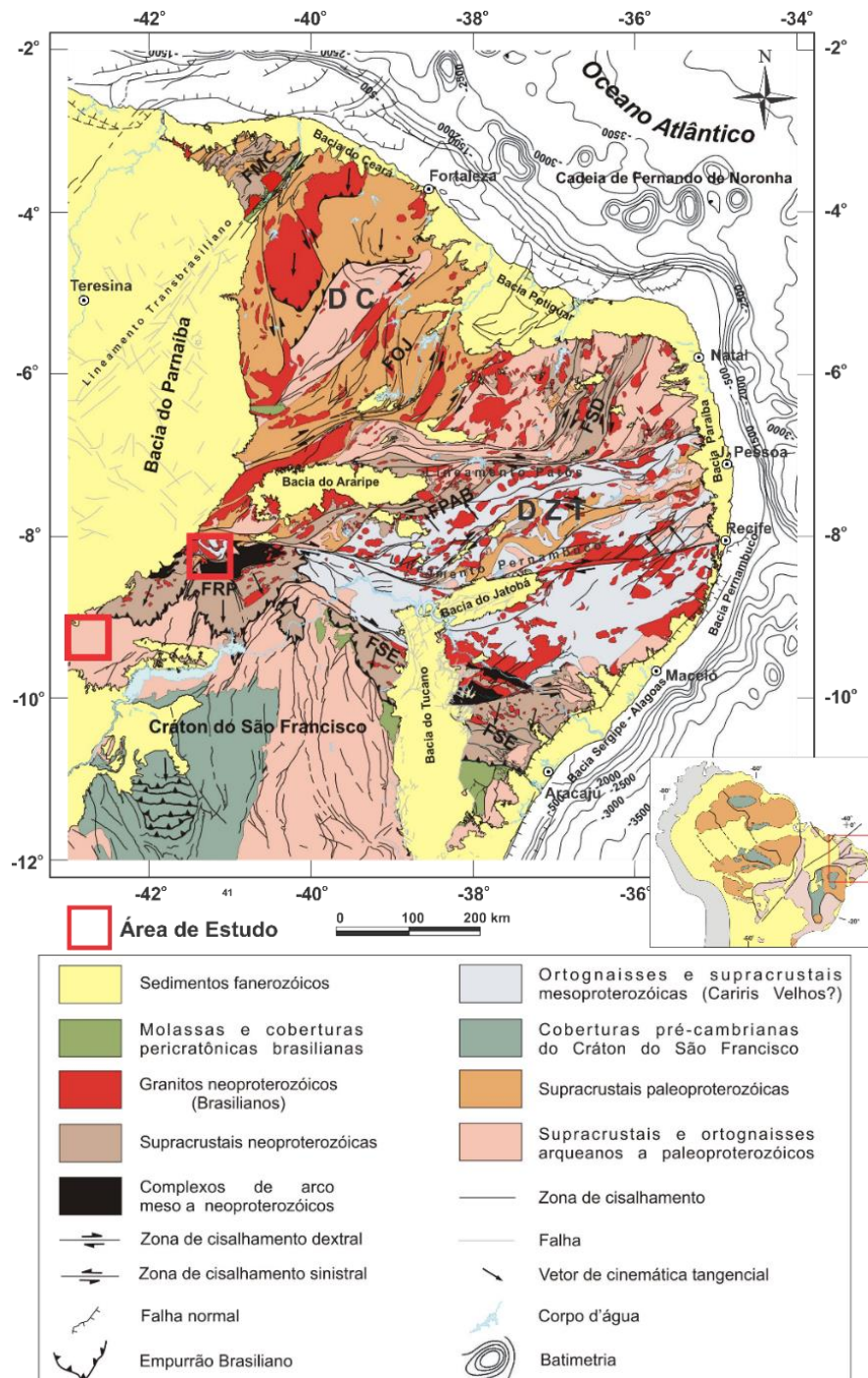
Figura 4: Mapa geológico da Província Borborema com a localização da área de estudo (modificado de Bizzi et al., 2003). Os retângulos em vermelho indicam as duas áreas de estudo.

_____

Capítulo 3

Manuscrito submetido à revista *Geophysics*

_____

"Can Euler Deconvolution outline 3D magnetic sources?"

CAN EULER DECONVOLUTION OUTLINE
3D MAGNETIC SOURCES?

Elizangela S. Amaral Mota. (1)(2), Walter E. Medeiros (1)(3)(4)(5),
and Roberto G. Oliveira (6)

(1) Programa de Pós-graduação em Geodinâmica e Geofísica. Centro de Ciências Exatas e da Terra. Universidade Federal do Rio Grande do Norte/UFRN. Natal/RN, Brazil. CEP 59.072-970.

(2) CPRM-Serviço Geológico do Brasil, Rua Goiás, 312, Frei Serafim, Teresina/PI, Brazil. CEP 64.001-620.

(3) Departamento de Geofísica. Centro de Ciências Exatas e da Terra. Universidade Federal do Rio Grande do Norte/UFRN. Natal/RN, Brazil. CEP 59.072-970.

(4) INCT-GP/CNPq. Instituto Nacional de Ciência e Tecnologia em Geofísica do Petróleo.

(5) Corresponding author.

(6) CPRM-Serviço Geológico do Brasil, Av. Sul, 2291, Afogados, Recife/PE, Brazil. CEP 50.770-011.

E-mails: elizangela.amaral@cprm.gov.br

walter.ufrn@gmail.com

roberto.gusmao@cprm.gov.br

ABSTRACT

Methodological researches have pointed out severe limitations of Euler deconvolution (ED) to outline source shape. However ED has been extensively employed on field data to outline interfaces and estimate dips of faults and shear zones, evidencing a disagreement between theoretical and practical results of the tool. To reconcile this disagreement, we show that ED might help to infer useful information about source volume and dip, when it is applied to the reduced-to-the-pole anomalies caused by two types of body. In the first, the body might have uniform magnetization contrast but rough interfaces. The dip can then be grossly estimated from the solution cluster. In the second type, the body interfaces might be smooth but it has internal magnetization contrasts. Now, besides dip, one can delimit approximately the source volume from the solution cluster envelope. ED was also applied to field anomalies, which are caused by a curved-shape thrust zone and by a banded iron formation. These two field cases were considered as examples of anomalies caused by the described first and second types of bodies, being the ED results similar for each body type: for the thrust zone, the solution cluster follows its known geologic shape and allows to estimate dip variation whilst, for the banded iron formation, the solution cluster spreads out occupying a volume. For the latter case, a trial-and-error 3D modeling of the field anomaly was also performed to estimate the magnetization distribution and ED was applied to the fitting synthetic anomaly. The resulting solution cluster is similar to the one obtained with the field anomaly, showing the consistency of the ED results. From the obtained results, it can be conclude that although ED does not outlines source shape it can furnish useful information about source dip and volume.

Keywords: Magnetometry; Euler deconvolution; magnetic modeling.

INTRODUCTION

Estimating shape and magnetization contrast of anomalous sources is a difficult task because of the inherent ambiguity of magnetic data inversion (Blakely, 1996). Thus, quantitative interpretation should be done ideally under the interpreter control. However, trial-and-error modeling approaches, particularly in the 3D case, is still a very time-consuming operation, especially when one takes into account the huge amount of data that the interpreter usually has to deal. As a result, semi-automatic inversion methods are the approach of choice at least for a first fast-track phase of the quantitative interpretation. Among these methods, one of the most used is the Euler Deconvolution (ED) proposed in the seminal work of Thompson (1982), which was generalized to the 3D case by Reid et al. (1990). ED allows to estimate simultaneously position and type of a magnetic source, being the type defined by a structural index (SI) associated with the decay rate of the magnetic anomaly.

ED has been extended to the gravity case (e.g. Zhang et al., 2000; Reid, et al., 2003) and has been widely used to interpret potential field data in several geological problems. A literature survey allows one to find applications as varied as: detecting lineaments, faults, trends, and/or geological contacts (Ferracioli et al., 2002; Oruç and Keskinsezer, 2008; Reeh et al., 2008; El-Gout et al., 2010; Oruç and Selim, 2011; Araffa et al., 2012; Gohl et al., 2013; Al-Saud. 2014; Rocha et al., 2014; Araffa et al., 2015; Hadhemi et al., 2016; Wang et al., 2017; Martins-Ferreira et al., 2018; Weiherman et al., 2018), locating suture zones (Bournas et al., 2003), estimating fault parameters (Ndougsa-Mbarga et al., 2012; Chen et al., 2014; Harrouchi et al., 2016; Khalil et al., 2016; Awoyemi et al., 2017; Bahrudin and Hamzah, 2018), locating faults to allow correlation with hypocenters in the case of seismogenic structures (Mazabraud et al., 2005; Minelli et al., 2016), delineating structures and/or tectonic blocks in sedimentary basins (Anand et al., 2009; Chandrasekhar et al., 2009; Ferraciolli et al., 2009; Castro 2011; Cooper et al., 2011; Castro et al., 2014; Dhaoui et al., 2014; Curto et al., 2015; Sridhar et al., 2017), outlining impact structures (Werner et al., 2010), characterizing iron-bearing zones or bodies (Mieth et al., 2014; Alamdar et al., 2015; Alamdar, 2016; Oladunjoye et al, 2016; Moghtaderi et al., 2017; Olasunkami et al., 2017), locating crustal anomalous bodies (Ebbing et al., 2007; Alrefae et al., 2017), and mapping basement structures in Precambrian areas (Osinowo et al., 2014; Zhang et al., 2015; Akinlalu et al., 2018; Ibraheem et al., 2018).

Since its proposition, potentialities and limitations of ED have been thoroughly discussed and several improvements were proposed (e.g. Barbosa et al., 1999; Barbosa et al., 2000; Silva et al., 2001; Reid, 2003; Cooper, 2004; FitzGerald et al., 2004; Mushayandebvu, 2004; Barbosa and Silva, 2005; Fedi, 2013; Melo et al., 2013; Guoqing, 2014; Melo and Barbosa, 2017). In particular the original ED has deficiencies associated to the presence of spurious solutions (e.g. Barbosa and Silva, 2005) and difficulties to estimate SI (e.g. Silva et al., 2001). In addition it has been argued that ED cannot outline 3D sources (Uieda et al., 2014) or even estimate source dips (e.g. Barbosa and Silva, 2005).

The presence of spurious solutions has been mitigated by the usage of additional restrictive criteria to accept solutions (e.g. Reid et al., 1990; Fairhead et al., 1994; Barbosa et al., 1999; Mikhailov et al., 2003; Melo et al., 2013). The difficulty in estimating SI was reduced after Barbosa et al. (1999) showed that a good choice for SI is that one producing the least correlation between the magnetic anomaly and a constant base level, which is a local approximation for the regional magnetic field. An alternative approach is the Hsu (2002) proposal of joint inversion of SI and source position. Finally, in order to obtain estimates of source dips, extensions of ED have been proposed (e.g. Mushayandebvu et al., 2001; Mushayandebvu et al., 2004; Ugalde and Morris, 2010; Guoqing, 2014).

Let us focus on the question of the inefficacy of ED to outline 3D sources. This inefficacy was evidenced by several theoretical studies as, for example, by Uieda et al. (2014) based on empirical results of ED obtained with magnetic sources of simple shape and uniform magnetization. On the other hand, contrasting results have been reported from ED applications on field data. As examples, ED has been used to outline in vertical sections faults and geological contacts (Fais et al., 1994; Widiwijayanti et al., 2004; Pilkington et al., 2009; Carvalho et al., 2012; Jordan et al., 2013; Carvalho et al., 2014; Sanchez-Rojas et al., 2014), delineate crustal-scale faults along transects (Curto et al., 2015; Zhang et al., 2015), estimate fault dips (Ndougsa-Mbarga et al., 2012; Bahrudin and Hamzah, 2018), and even to sketch the 3D architecture of sedimentary basins (Castro, 2011; Rodrigues et al., 2014) or to model a 3D fault system (Jammes et al., 2010; Rabii et al., 2018). Therefore, it can be seen that there is a disagreement between the theoretical and practical results of ED about its efficacy to outline 3D sources.

In our view, the referred disagreement is related to the question of whether theoretical models actually typify real geological bodies. Geological bodies might have

characteristics rarely (or hardly) incorporated in theoretical models, as high interface roughness and intense variation of magnetization. In this work we apply ED to two types of bodies where we incorporate these two characteristics in the simplest possible manners. In the first one, we take into account interface roughness by employing anomalous bodies which have uniform contrast of magnetization but delimiting interfaces containing several edges. On the other hand, in the second type of body, the delimiting interfaces are dominantly smooth but the magnetization intensity varies inside the body. As we show, the obtained results with ED, applied in the reduced-to-the-pole version of the anomalies, although do not outline accurately the sources, indeed allow the interpreter to infer useful information about their dip and volume.

We also apply ED to two aeromagnetic field anomalies, which were judiciously chosen in a large survey area in Piauí state, Brazil (Figure 1), as field cases as close as possible to the two referred types of anomalous bodies, according to the available geological information. For each case, the ED result obtained with field data is similar to that one obtained with the respective type of synthetic data. Below, we begin by presenting a summary of the employed methodology and, later, we show the applications of ED for synthetic and field anomalies.

METHODOLOGY

The methodology is composed by the following elements: a) 3D magnetic modeling in the case of synthetic anomalies and, both in synthetic and field data cases, b) reduction to the pole transformation, c) application of the ED classic version (Reid et al., 1990) using an industry tool, and d) elimination of spurious solutions.

3D magnetic modeling

The magnetic modeling was done using the approach of Okabe (1979). Based on the superposition principle and combining the Poisson theorem and Green's third identity, Okabe (1979) deduced an analytical closed expression for the magnetic field produced by a polyhedral body having polygonal facets and uniform magnetization. An algorithm based on this expression allows to compute the magnetic anomaly of complex-shaped bodies having uniform magnetization. In addition, by superposing the effects of multiple bodies, it is possible to vary also the magnetization. For simplicity, the effects of

remanence were not taken into account so that the resulting magnetization is assumed to be induced, even in the 3D trial-and-error modeling of field data.

The magnetic anomaly of all synthetic bodies were calculated using the typical magnetic environment of the survey area in the Piauí state, Brazil (Figure 1): inclination and declination equal to -23º and -22º, respectively. The survey area is part of the Borborema Province, a major geologic/tectonic unity located in the Northeastern region of Brazil (Almeida et al., 1981). The strike of all bodies was chosen to be N60ºE, because this is the dominant direction of shear zones, related emplaced bodies, and associated magnetic anomalies in the study area (Oliveira and Medeiros, 2018), as a result of the Pan-African/Brasiliano tectonic event that occurred during the West Gondwana amalgamation (Brito Neves et al., 1999; Arthaud et al., 2008).

Reduction to the pole transformation

The interpretation of magnetic anomalies is facilitated when they are reduced to the pole, because in this condition the anomaly peak is positioned over the magnetic source and source dips are more evident (Blakely, 1996). In addition, ED presents better performance when it is applied to the reduced-to-the-pole version of the anomalies (Thompson, 1982). We follow then the common procedure of applying this transformation as a previous step to ED.

Reduction to the pole might be an unstable transformation in low-latitude regions (Silva, 1986), because spurious magnetic lineaments might be generated along the direction of declination. As informed above, inclination is typically equal to -23º. For this inclination, we verified using synthetic data that spurious effects caused by reduction to the pole are indeed present. However, they can be greatly mitigated by employing the pseudo-inclination method (MacLeod et al., 1993).

Euler deconvolution

ED is based on the Euler's homogeneity equation given by (Blakely, 1996):

$$(\vec{r} - \vec{r}_0).\vec{\nabla}T = -\eta T \qquad \text{(Eq. 1)}$$

where T is the magnetic anomalous field measured at the point $\vec{r}$, which is caused by a source located at the point $\vec{r}_0$, being η the decay rate of the generated anomaly. η is known as the structural index (SI) (Thompson, 1982). For example, $\eta = 3$ corresponds to a point dipole, $\eta = 2$ corresponds to a line of dipoles, and $\eta = 1$ is associated with a thin, dipping

prism. Fractional SI values are sometimes used (e.g. Reid et al., 1990; Castro, 2011) as a manner of mitigating solution spreading.

When referred to a right-hand Cartesian coordinate system with x, y, and z axes pointing in the North, East, and down directions, respectively, ED can be written as (Thompson, 1982):

$$(x - x_0)\frac{\partial T}{\partial x} + (y - y_0)\frac{\partial T}{\partial y} + (z - z_0)\frac{\partial T}{\partial z} = -\eta(T - B) \, , \quad \text{Eq.} \quad (2)$$

where $(x, y, z) = \vec{r}$, $(x_0, y_0, z_0) = \vec{r}_0$, and a base level B was included to represent locally the regional component of the magnetic field (Reid et al., 1990; Barbosa et al., 1999).

Acceptance criteria for the solutions

Eq. 2 is valid at every point (x, y, z). However, given a SI, Eq. 2 is often solved in the least-squares sense for the field dataset contained in a given window in order to obtain reliable estimates of (x_0, y_0, z_0) and B. The Moore-Penrose inversion (Reid et al., 1990) might be employed to stabilize the solutions. The window is moved and, depending on the overlapping between adjacent windows, several estimates might be obtained for the same source point (x_0, y_0, z_0), from which mean and variation around the mean can be estimated (Reid et al., 1990).

ED solutions are often too scattered so that posterior acceptance criteria are necessary. We employ two acceptance criteria. The first one, from now on named Depth-filtering, is the criterion described in Reid et al. (1990) that, for a set of estimates of (x_0, y_0, z_0), retain just the estimates whose depth uncertainty is limited to a given percentage of the mean value (often the chosen value is lower than 15%). Table 1 shows the parameters used in the ED for all synthetic and field cases. The second criterion, henceforth named as Volume-filtering, is always applied after the Depth-filtering. It is a simple empirical criterion we developed and consists in discarding the solutions which are located outside a given oblique prism defined by eight vertices (Figure 2). The top and bottom faces of the prism are parallel to the Earth's surface and might be rectangles or rhombuses. The prism dimensions and dip (angle α in Figure 2) are inferred from the visual analysis of both the ED solution cluster and the reduced-to-the-pole anomaly so that, according to the interpreter appraisal, the prism contains the acceptable solutions. In particular, the prism horizontal dimensions must be large enough to contain the cluster of shallowest solutions that delineate the upper face of the magnetic source.

RESULTS FOR SYNTHETIC DATA

Figure 3a shows the anomalous Body A which has uniform contrast of magnetization (1.0 A/m), in relation to the surrounding medium, but rough delimiting interfaces. On the other hand, Figure 3b shows the anomalous Body B whose delimiting interfaces are smooth but has strong internal contrasts of magnetization. In Figure 3b note that the magnetization intensity inside each prism is cumulative; that is, the magnetization intensities relative to the surrounding medium is 1.0 A/m and 5.2 A/m for the outermost (in black) and innermost (in green) prisms, respectively.

The depths of the source tops are 1.5 km and 0.5 km for bodies A and B, respectively. On the other hand, the depth of the source bottom is 5.5 km for both bodies. Body A might represent, for example, a sheet of anomalous material emplaced in a transtractive sector or crushed/squeezed in a compressive sector of a shear zone. On the other hand, Body B might represent a massive concentration of iron ore.

The anomalous fields caused by bodies A and B were calculated on a grid on the Earth surface having dimensions 40 km (E-W) and 30 km (S-N). The grid size is 100 m in both directions. The resulting datasets were interpolated using the minimum-curvature method. After the reduction to the pole transformation, the anomaly caused by Body A is shown in Figure 4a, that shows also the projections on the Earth's surface of the body edges. Observe that the body strike (N60^{o}E) is clear in the anomaly shape. In addition, the body dip to SE (Figure 3a) can be inferred from the anomaly asymmetry along the direction perpendicular to the body strike.

Based on the source shape, we select a priori SI equal to 1 for Body A. After applying just the Depth-filtering criterion, ED solutions are shown as a 3D view in Figure 5a. From this figure, it is clear that the solutions are not restricted to the top of the source. Although the depth of the source bottom is 5.5 km, there are consistent ED solutions up to 4.5 km (Figure 5a). Note that a subset of the ED solution cluster forms a ramp, which follows grossly the ladder defined by the edges of Body A, while another subset forms complex 3D shapes. The role of the second acceptance criterion of solutions (Filtering-volume) is to eliminate as much as possible the subset of solutions forming these complex 3D shapes. Figure 5b shows the ED solutions, already presented in Figure 5a, now in a joint view with the prism used to filter them. After applying the Filtering-volume criterion, the remaining solutions are shown alone in Figure 5c, in a joint 3D view with Body A in Figure 5d, and superposed on the magnetic anomaly in Figure 4b.

To better analyze the discrepancy between the body dip and the dip associated with the cluster of ED solutions, we show in Figure 6 the results of additional tests, employing the same SI and similar bodies, but modifying the dip of the ladder formed by the edges. Note that Figure 6 shows views on the vertical section perpendicular to the body strike and that Body A is the case (b) of this figure. From these results one can conclude that the resolution on the dip estimate might be poor; however, even in the worst cases at least the dip direction is safely estimated.

As a final test to evidence that the ED solution cluster is really associated with the non-smooth boundaries of the body, we show in Figure 7 the results of three additional tests: now we gradually remove the composing bodies, one pair at a time, starting with the deepest pair. Accordingly, the resulting number of solutions composing the ED clusters decreases gradually, from bottom to top. Note also that the discrepancy of the dip estimates varies.

For Body B, the reduced-to-the-pole version of the anomaly is shown in Figure 8a. This figure also shows the projections on the Earth's surface of the body edges, including the internal ones. Similarly to Body A, the body strike (N60°E) is clear in the anomaly shape. However, now the anomaly is almost symmetric in relation to its central axis following the strike direction, thus revealing that the magnetization distribution inside the body is also approximately symmetric. In particular, the dip (or at least, the mean dip) is subvertical.

On the contrary of Body A, it is not easy to select an a priori value to SI in the case of Body B. To confirm the difficulty, we present in Table 2 the results of tests to select SI values based on the criteria of minimizing the variations of either the base level and depth estimates (Melo and Barbosa, 2017a and b). The two SI selection criteria produce the same results (SI = 3). However, we performed three additional tests where the internal bodies were removed, one by one, from the bottom up. Although the two criteria suggest the same SI values for each resulting anomaly, the suggested value changes as the internal magnetization contrasts are removed (Table 2).

Because of the difficulty in selecting SI, we decide to apply ED with all three possible integer values. The resulting ED solutions are shown in Figures 9a, 10a, and 11a for SI equal, to 1, 2, and 3, respectively. The cluster for SI equal to 3 is also shown as projections on the Earth's surface in Figure 8b, superposed on the magnetic anomaly. Observe that all ED clusters contain solutions that are not restricted to the top of the source (Figures 9a, 10a, and 11a), in a similar manner to the results for Body A. Inspecting

the clusters of solutions one can infer, independently of the employed SI, that the body dip is subvertical, in a consistent way with the anomaly symmetry. In addition, there are very deep ED solutions for all SI, so that (except near its NE and SW vertical faces) the internal volume of the body is partially occupied by solutions, particularly for SI equal to 1 or 2. Thus, a gross estimate of the source volume might be obtained from the surface enveloping the ED solution cluster.

To confirm that the presence of the deep solutions in Figure 9a is due to the strong internal contrasts of magnetization (Figure 3b), we show in Figures 9b-9d the results of three ED additional tests also using SI = 1 and applying the same window parameters (Table 1), but now removing the internal bodies one by one from the bottom up. Note that the subset of deep solutions gradually decreases, so that in the last case (Figure 9d), when just the outermost body (Figure 3b) is maintained, the solutions practically outline just the top of the body. ED solution clusters for similar triads of tests are shown in Figures 10b-10d for SI = 2 and in Figures 11b-11d for SI = 3. Qualitatively the results are similar independently of the used SI.

Summarizing the results obtained with synthetic bodies A and B, we can say, in strict words, that ED does not really outlines 3D magnetic sources. In fact, except for the top face of the bodies, the delimiting interfaces were not delineated in any modeled case. However, reliable and useful information about dip (at least dip direction in the worst case) and/or source volume might be indeed inferred for both cases.

RESULTS FOR FIELD DATA

We also apply ED to two aeromagnetic field anomalies, which were judiciously chosen in a large survey area in Piauí state, Brazil (Figure 1) in order that their sources conform as much as possible, accordingly to the know geological information, to the two types of synthetic anomalous bodies above presented. The first anomaly (Figure 12), henceforth named as Paulistana anomaly, is associated with a curved-shape thrust shear zone (Figure 13). This anomaly might be explained by a thin sheet of anomalous material crushed/squeezed inside the thrust shear zone, being thus similar to the one caused by synthetic Body A (Figure 3a). On the other hand, the second anomaly (Figure 14), henceforth named as the São Raimundo Nonato anomaly, is caused by a massive concentration of iron ore inside banded iron formations contained in a meta-volcano-metasedimentary sequence (Figure 15). This anomaly is then similar to the one caused by

synthetic Body B (Figure 3b). Note that both shown anomalies (Figures 12 and 14) are not yet reduced to the pole.

Aeromagnetic survey information

The two chosen anomalies are included in a large surveyed area covering the Southeastern region of Piauí state (Figure 1) and adjacent regions of the neighboring states (Ceará, to the East and Pernambuco, to the South). For the two chosen anomalies, the flight height was 100 m and the survey lines were oriented in the N-S direction. Total field measurements with cesium-vapor magnetometers were done every 0.1 s along the survey lines, which is equivalent to every 7.7 m on the ground. The tie lines were spaced by 500 m. The GPS positioning accuracy is about 1.0 m. State-of-the-art data processing (including IGRF removal) was performed by the firms contracted for the surveys, resulting high precision magnetic anomalous field datasets as one can appreciate in Figures 12 and 14. The only processing operation we applied before ED was reduction to the pole transformation.

Paulistana anomaly - thrust shear zone

This study area is part of the Riacho do Pontal belt, near the limit between the Borborema Province and the São Francisco craton. The Riacho do Pontal belt suffered in the Neoproterozoic intense deformation associated with the Pan-African/Brasiliano orogeny, which occurred during the West Gondwana amalgamation (Brito Neves et al., 1999; Arthaud et al., 2008). Nappes of the Riacho do Pontal belt are identified as vestiges of the thrusting process of the Borborema Province over the São Francisco craton (Oliveira and Medeiros, 2018). In the Paulistana area, a crustal fragment was thrusted to the South, forming a curved-shape shear zone (Figure 13). The shear zone dip to the North and the dip angle is low, frequently near 20º but varying between 5º and 40º (Uchôa Filho and Freitas, 2017). In the reduced-to-the-pole version of the magnetic anomaly (Figure 16a) the trace on the Earth's surface of the thrust zone was added, so that one can verify that this anomaly is really associated with this shear zone (possibly a sheet of squeezed anomalous material).

After applying both the Depth- and Filtering-volume criteria, the resulting ED cluster of solutions is shown in Figure 16b superposed to the magnetic anomaly. We select $SI = 1$ because the causative body might be considered as a dipping curved-shaped thin dike. Note that the solution cluster follows the thrust zone, a fact that is better appreciated

in Figure 17, where the dipping for North (that is, ranging from NE to NW) of the solution cluster can also be seen. Note also that the cluster includes solutions as shallow as 80 m, in accordance with the fact that the thrust shear zone is outcropping (Figure 13). To better analyze the dip estimates which can be obtained from the ED solutions, Figure 18a shows a 3D view of the solutions whilst Figures 18b, 18c, and 18d show the solutions subsets which are concentrated near the vertical planes containing the three transversal profiles L1, L2, and L3, respectively (the positions of the three profiles are shown in Figure 18a). Observe in Figures 18b, 18c, and 18d that every dip estimate is around 20º, in accordance with the known geological information (Uchôa Filho and Freitas, 2017).

Similar results to the above described for the Paulistana anomaly were obtained by Gopal (2016) for thrust zones in the Himalayas. Several other ED applications also report dip estimates for geological structures (e.g. Rodrigues et al., 2014; Zhang et al., 2015; Bahrundin and Hamzam, 2018)

São Raimundo Nonato anomaly - massive concentrations of iron ore
In this area a Neoarchean meta-volcano-sedimentary sequence occurs (Figure 15). The basement are formed by migmatitic orthogneisses of Paleoproterozoic age (Figure 15). The meta-volcano-sedimentary sequence includes banded iron formations (the Lagoa do Alegre and Lagoa da Ema complexes), which have zones containing massive concentrations of iron ore. The chosen magnetic anomaly (Figure 14) is caused by a zone of this kind, according both to the surface geology information (Augusto et al., 2014) and drilling holes (Cordani, 2013). Therefore, we consider this anomaly is being similar to the one caused by synthetic Body B (Figure 3b).

A reduced-to-the-pole version of the magnetic anomaly is shown in Figure 19a, superposed to the available geological information. A visual inspection of this anomaly allows one to infer that its causative body: a) strikes in NE directions, b) has width approximately equal to 850 m, c) has subvertical dip (because of the anomaly symmetry), d) has a deeper upper face in its southwestern end part, and e) is possibly cut by a NW-SE sinistral strike-slip fault offsetting its southwestern end part from the remaining part (Figure 19b). It is known that this fault has a normal component (Augusto et al., 2014). We assign the depth change of the upper face of the body to the normal component of this fault.

We tested three different SI values (1, 2, and 3), choosing SI = 3 because it produces base level estimates showing the smallest standard deviation, following in this

way the recommendation of Melo and Barbosa (2017a) to choose the SI in cases where the interest anomaly suffers the effects of interfering bodies. Note that the same SI value resulted from the application of this criterion to the anomaly caused by Body B (Table 2).

After applying both the Depth- and Filtering-volume criteria, the resulting ED cluster of solutions is shown in Figure 19b, over the reduced-to-the-pole version of the magnetic anomaly, and as a 3D view in Figure 20. From these figures one can infer that the ED solutions, although follow grossly the anomaly contours (Figure 19b), vary from very shallow (< 150 m) to very deep (around 700 m) (Figure 20). In their spatial distribution, note that there is a relatively higher concentration of deep solutions in the southwestern part of the anomaly (compare the number of yellow and red points in Figure 19b), in accordance with the previous analysis that there the upper face of the causative body is deeper. More important, although the drill holes shown in Figure 19a have approximately the same length, drill holes 4 and 5 did not reach the causative body but drill holes 1, 2 and 3 found it (Cordani, 2013). Therefore, we cannot consider the deep elements of the ED cluster of solutions as spurious because they are consistent with all available information. In the following we give further arguments favouring the reliability of these solutions.

We performed a trial-and-error 3D modeling of the magnetic anomaly using the Okabe (1979) method, under the assumption that the magnetization is induced. The resulting estimated model is shown in Figure 21 as a projection on the Earth's surface over the generated synthetic magnetic anomaly, and in Figure 22 as a 3D view, either alone (Figure 22a) or together (Figure 22b) with the ED solution cluster obtained with the field anomaly (Figure 20). Note that: a) the body strikes approximately in the direction N75°E, b) the body dip is subvertical, c) the shallowest part of the upper face of the body has depth equal to 100 m, d) there are strong internal contrasts of magnetization (in a similar manner to the synthetic Body B, the contrasts shown in Figure 22a are cumulative), e) the body has an offset between its southwestern and northeastern parts, coinciding approximately with the position of the inferred NW-SE sinistral strike-slip fault (Figure 19a), f) the upper face of the body is deeper in its southwestern part, g) the intensity of magnetization increases more sharply in the northeastern end part of the body than in the southwestern end part, and h) the modeled outermost body contains approximately all elements of the solution cluster (Figure 22b). By this way, all available geophysical and geological information, including the constraint that the source volume contains approximately the ED solution cluster, were incorporated in the model.

The generated synthetic anomaly (Figure 21) fits quite well the field anomaly (Figure 19a), as one can verify by comparing these two figures, or by comparing the profiles L1 to L5 (Figures 23a to 23e). Discarding the effects of laterally interfering bodies, the only part of the anomaly in which the misfit is relatively high is along the L1 profile (Figure 23a) evidencing that the magnetization increase in the southwestern end part of the body should be even more gradual than the modeled one. Given the small misfit between field and synthetic anomalies, we applied ED to the latter one using the same SI, parameters and solution acceptance criteria employed for the field anomaly (Table 2). The resulting ED cluster of solutions is shown in Figure 24 superposed to the synthetic anomaly and in Figure 25 in a 3D view jointly with the modeled body. Note that the ED solution cluster resulting from the synthetic anomaly reproduces qualitatively all the main characteristics described previously for the ED solution cluster resulting from the field anomaly (compare Figures 19b and 24, or Figures 22b and 25). We conclude then the ED solution cluster (Figure 19b) is reliable and really results from the internal contrasts of magnetization.

DISCUSSION

Let us first give qualitative mathematical arguments to support the results. Eq. 1 (or its version for the Cartesian coordinate system given by Eq. 2) is valid at every measuring point. However, Eq. 2 is often solved in the least-squares sense, using the field dataset of a mesh contained in a window. The resulting Gramm operator is increasingly diagonally dominant as the window size increases and the mesh size decreases; in the limit when the window size tends to infinity and the mesh size tends to zero, the Gramm operator is exactly diagonal as shown by Barbosa et al. (1999). Let us examine the terms of the ED least squares-equation, assuming that the window is large enough for the Gramm operator to be strongly diagonally dominant, so that the effects of its off-diagonal entries can be discarded. In this condition, the eingenvalues of the Gramm operator are equal to its diagonal elements. We assume initially that the source is a vertical prism of uniform contrast of magnetization, producing magnetic anomalies as the ones shown in Figures 26a and 26g. Later more complex bodies will be considered.

The diagonal elements of the Gramm operator are the three Cartesian terms of $\left\|\vec{\nabla}T\right\|^2$, that is $(\frac{\partial T}{\partial x})^2$, $(\frac{\partial T}{\partial y})^2$, and $(\frac{\partial T}{\partial z})^2$, besides $N\eta^2$, where N is number of mesh points

contained in the window. On the other hand, the entries of the right-hand side of the ED least-squares equation contain elements of the form $\left\langle \frac{\partial T}{\partial \alpha} \Big| \alpha \frac{\partial T}{\partial \alpha} \right\rangle$ and $\beta \left\langle \frac{\partial T}{\partial \alpha} \Big| \frac{\partial T}{\partial \beta} \right\rangle$, where α and β stand generically for x, y, and z, being $\alpha \neq \beta$, and $\langle . | . \rangle$ represents the inner product of the quantities inside the window (Barbosa et al., 1999). As a result, regions having high values of $\left\| \vec{\nabla} T \right\|^2$ contribute dominantly to form both the eingenvalues of the Gramm operator and the entries of the right-hand side of the ED least-squares equation. Because x and y define the Earth's surface, where the measurements are done, components x and y of $\vec{\nabla} T$ are very well sampled and have high values over the top face borders of the prisms (Figures 26b and 26h). On the other hand, the z-component of $\vec{\nabla} T$, as estimated from measurements on the x-y plane, is relatively high over the prism center (Figures 26c and 26i). However, in comparison with the x- and y-components, the effects in the z-component is lower, being much more sensitive to the depth of the top than to the depth of the bottom of the prism. As consequence, the ED solutions are highly biased by the contributions for $\vec{\nabla} T$ caused by the prism upper face. For example, doubling the prism thickness produces significant effects in the x-component of $\vec{\nabla} T$ (compare Figures 26b and 26h) but almost negligible effects in the z-component of $\vec{\nabla} T$ (compare Figures 26c and 26i). Therefore, ED solutions are actually equivalent solutions honoring almost exclusively the dominant effects of the upper part of the prism (compare Figures 26d and 26j).

The rationale above explains why ED is so successful in outlining the contour of the upper face of magnetic sources: compared to all other faces, the shape and gradients of the magnetic anomaly register very well the details of the source upper face. Concerning the other faces of the source, there are basically two cases where their effects on the anomaly gradient measured on the Earth's surface might increase: if the source has dipping and rough delimiting interfaces (containing edges, saliences, or protuberances, for example), and/or if the source has strong internal contrasts of magnetization (produced either by remanence and intensity variation). This is the kind of result we show here with both synthetic and field data.

Comparing however the degree of agreement between each pair of ED results for the synthetic and field anomalies we consider as being similar (that is, Body A and Paulistana anomalies, for dipping rough interfaces, and Body B and São Raimundo Nonato anomalies, for strong internal contrasts of magnetization), we evaluate that we

were comparatively much more successful with the second pair. In other words, with the simple modeling approach through which we tried to typify real geological bodies, we came closer to mimic real strong internal contrasts of magnetization but we are still far from modeling real dipping rough interfaces. Actually, rough surfaces in Nature might be even fractals and not just simple edges as we modeled here.

Despite the difference in success in modeling the two types of bodies, in both cases one can state, at least, that ED allows the interpreter to infer more information about a real source than just outlining its upper face contour. The ED practitioners learned this rapidly based on their large experience in dealing with field data and comparing ED results with available geological information. So, practitioners are one step ahead of theorists in this matter. To confirm the practitioners view, we employ here an ED version as close as possible to what they do (that is, a classic ED provided by a standard industry tool) and we work just in the direction of trying to typify as far as possible real geological bodies with the available modeling algorithms.

CONCLUSIONS

There is a disagreement in the literature between theoretical and practical results of ED concerning its efficacy to outline 3D magnetic sources. In our view, this disagreement can be resolved by recognizing that theoretical models are still very far from typifying real geological bodies, because these bodies might have characteristics rarely (and hardly) incorporated in the models as, for example, high interface roughness and intense variation of magnetization. In this work we apply ED to synthetic magnetic anomalies produced by two types of models incorporating in a simple manner these two characteristics. We also apply ED to two aeromagnetic field anomalies, which were judiciously chosen as field cases as close as possible to these two types of anomalous bodies, according to the available geological information. The obtained results with ED, applied in the reduced-to-the-pole version of the anomalies, were similar both for synthetic and field datasets, particularly for the case of anomalous bodies having strong internal contrasts of magnetization. For the models we employed, ED does not really outlines 3D magnetic sources. However, even for these models still very simple, ED allows the interpreter to infer more information about the magnetic sources than just outlining their upper face boundaries. In fact, useful additional information about dip and source volume can be

inferred if the source delimiting interfaces are very rough and/or the source has strong internal contrasts of magnetization.

ACKNOWLEDGMENTS

REFERENCES

Akinlalu, A.A., Adelusi, A.O., Olayanju, G.M., Adiat, K.A.N., Omosuyi, G.O., Anifowose, A.Y.B., Akeredolu, B.E., 2018. Aeromagnetic mapping of basement structures and mineralization characterisation of Ilesa Schist Belt, Southwestern Nigeria: Journal of South African Earth Sciences, **138**, 383-391.

Alamdar, K., 2016. Interpretation of the magnetic data from Shavaz iron ore using enhanced local wavenumber (ELW) and comparison with Euler deconvolution method: Arabian Journal of Geosciences, **9**: 597. https://doi.org/10.1007/s12517-016-2616-2.

Alamdar, K., Kamkare-Rouhani, A., Ansari, A.H., 2015. Interpretation of the magnetic data from anomaly 2c of Soork iron ore using the combination of the Euler deconvolution and TDX filter: Arabian Journal of Geosciences, **8**, 6021-6035.

Almeida, F.F.M., Hasui, Y., Brito Neves, B.B., Fuck, R.A., 1981. Brazilian structural provinces: An introduction. Earth-Science Review, **17**, 1-29.

Alrafaee, H.A., 2017. Crustal modeling of the central part of Northern Western Desert, Egypt using gravity data: Journal of African Earth Sciences, **129**, 72-81.

Al-Saud, M.M., 2014. The role of aeromagnetic data analysis (using 3D Euler deconvolution) in delineating active subsurface structures in the west central Arabian

shield and the central Red Sea, Saudi Arabia: Arabian Journal of Geosciences, **7**, 4361-4376.

Anand, S.P., Rajaram, M., Majumdar, T.J., Bhattacharyya, R., 2009. Structure and tectonics of 85°E Ridge from analysis of geopotential data: Tectonophysics, **478**, 100-110.

Araffa, S.A.S., Sabet, H.S., Gaweish, W.R., 2015. Integrated geophysical interpretation for delineating the structural elements and groundwater aquifers at central part of Sinai Peninsula, Egypt: Journal of South African Earth Sciences, **105**, 93-106.

Araffa, S.A.S., Santos, F.A.M., Arafa-Hamed, T., 2012. Delineating active faults by using integrated geophysical data at northeastern part of Cairo, Egypt: NRIAG Journal of Astronomy and Geophysics, **1**, 33-34.

Arthaud, M.H., Caby, R., Fuck, R.A., Dantas, E.L., Parente, C.V., 2008. Geology of the Northern Borborema Province, NE Brazil and its correlation with Nigeria, NW Africa. In: Pankhurst, R.J., Trouw, R.A.J., Brito Neves, B.B., De Wit, M.J. (Eds.), West Gondwana: Pre-Cenozoic Correlations Across the Atlantic Region: Geological Society, London, Special Publications, **294**, 49-67.

Augusto, G.G.S.; Santos, E. J., 2014. São Raimundo Nonato - Folha SC.23-X- D-II: Estado do Piauí. Carta Geológica. Teresina: CPRM, mapa, color, 91,04 x 65,84 cm. Escala 1:100.000: Programa Geologia do Brasil - PGB. (available at <geosgb.cprm.gov.br>).

Awoyemi, M.O., Hammed, O.S., Falade, S.C., Arogundade, A.B., Ajama, O.D., Iwalehin, P.O., Olurin, O.T., 2017. Geophysical investigation of the possible extension of Ifewara fault zone beyond Ilesa area, southwestern Nigeria: Arabian Journal of Geosciences, **10:** 27. https://doi.org/10.1007/s12517-016-2813-z.

Bahrudin, N.F.D.B., Hamzah, U., 2018. Fault lineaments and depth estimation by aeromagnetic data of Mersing Fault Zone in Johore, Peninsular Malaysia: ARPN Journal of Engineering and Applied Sciences, **13**, 2108-2115.

Barbosa, V.C.F., Silva, J.B.C, Medeiros, E.W., 1999. Stability analysis and improvement of structural index estimation in Euler deconvolution: Geophysics, **64**, 48-60.

Barbosa, V.C.F., Silva, J.B.C, Medeiros, E.W., 2000. Making Euler deconvolution applicable to small ground magnetic surveys: Journal of Applied Geophysics, **43**, 55-68.

Barbosa, V.C.F., Silva, J.B.C., 2005. Deconvolução de Euler: passado, presente e futuro - um tutorial: Revista Brasileira de Geofísica, **23**, 243-250.

Blakely, J.R., 1996. Potential Theory in Gravity and Magnetic Applications Cambridge University Press. Second Edition, p. 461.

Bournas, N., Galdeano, A., Hamoudi, M., Baker, H., 2003. Interpretation of the aeromagnetic map of Eastern Hoggar (Algeria) using the Euler deconvolution, analytic signal and local wavenumber methods: Journal of African Earth Sciences, **37**, 191-205.

Brito Neves, B.B., Campos Neto, M.C., Fuck, R.A., 1999. From Rodinia to Western Gondwana: an approach to the Brasiliano-Pan African Cycle and orogenic collage. Episodes, **22**, 155-166.

Carvalho, J., Matias, H., Rabeh, T., Menezes, P.T.L., Barbosa, V.C.F., 2012. Connecting onshore structures in the Algarve with the southern Portuguese continental margin: The Carcavai fault zone: Tectonophysics, **570-571**, 151-162.

Carvalho, J., Rabeh, T., Dias, R., Dias, R., Pinto, C., Oliveira, T., Cunha, T., Borges, J., 2014. Tectonic and neotectonic implications of a new basement map of the Lower Tagus Valley, Portugal: Tectonophysics, **617**, 88-100.

Castro, D.L., 2011. Gravity and magnetic joint modeling of the Potiguar Rift Basin (NE Brazil): Basement control during Neocomian extension and deformation: Journal of South American Earth Sciences, **31**, 186-198.

Castro, D.L., Fuck, R.A., Philips, J.D., Vidotti, R.M., Bezerra, F.H.R., Dantas, E.L., 2014. Crustal structure beneath the Paleozoic Parnaíba Basin revealed by airborne gravity and magnetic data, Brazil: Tectonophysics, **614**, 128-145.

Chandrasekhar, E., Fontes, S.L., Flexor, J.M., Rajaram, M., Anand, S.P., 2009. Magnetotelluric and aeromagnetic investigations for assessment of groundwater resources in Parnaiba basin in Piaui State of North-East Brazil: Journal of Applied Geophysics, **68**, 269-281.

Chen, Q., Dong, Y., Cheng, S., Han, L., Xu, H., Chen, H., 2014. Interpretation of fault system in the Tana Sag, Kenya, using edge recognition techniques and Euler deconvolution: Journal of Applied Geophysics, **109**, 150-161.

Cooper, G.R.J., 2004. Euler Deconvolution applied to potential field gradients: Exploration Geophysics, **35**, 165-170.

Cooper, S.M., Liu, T., 2011. A magnetic and gravity investigation of the Liberia Basin, West Africa: Journal of South African Earth Sciences, **59**, 159-167.

Cordani, R., 2013. Constraint modelling in iron ore exploration. 13th International Congress of the Brazilian Geophysical Society & EXPOGEF, SBGF, 702-704. https://doi.org/10.1190/sbgf2013-145.

Curto, J.B., Vidotti, R.M., Blakely, R.J., Fuck, R.A., 2015. Crustal framework of the northwest Paraná Basin, Brazil: Insights from joint modeling of magnetic and gravity data: Tectonophysics, **655**, 58-72.

Dhaoui, M., Gabtni, H., Jallouli, C., Jleilia, A., Mickus, K.L., Turki, M.M., 2014. Gravity analysis of the Precambrian basement topography associated with the northern boundary of Ghadames Basin (southern Tunisia): Journal of Applied Geophysics, **111**, 299-311.

Ebbing, J., Skilbrei, J.R., Olesen, O., 2007. Insights into the magmatic architecture of the Oslo Graben by petrophysically constrained analysis of the gravity and magnetic field: Journal of Geophysical of Research, **112**, B04404. https://doi:10.1029/2006JB004694.

El Gout, R., Khattach, D., Houari, Mohammed-Rachid, Kaufmann, O., Aqil, H., 2010. Main structural lineaments of north-eastern Morocco derived from gravity and aeromagnetic data: Journal of South African Earth Sciences, **58**, 255-271.

Fairhead, J.D., Bennett, K.J., Gordon, D.R.H., Huang, D., 1994. Euler: Beyond the "Black Box". SEG Technical Program Expanded Abstracts, 422-424. https://doi.org/10.1190/1.1932113.

Fais, S., Klingele, E.E., Tocco, R., 1994. Geophysical interpretation of the Gallura magnetic anomaly (northeast Sardinia, Italy): Tectonophysics, **233**, 125-144.

Fedi, M., Florio, G. 2013. Determination of the maximum-depth to potential field sources by a maximum structural index method: Journal of Applied Geophysics, **88**, 154-160.

Ferraccioli, F., Armadillo, E., Jordan, T., Bozzo, E., Corr, H., 2009. Aeromagnetic exploration over the East Antarctic Ice Sheet: A new view of the Wilkes Subglacial Basin: Tectonophysics, **478**, 62-77.

Ferraccioli, F., Bozzo, E., Damaske, D., 2002. Aeromagnetic signatures over western Marie Byrd Land provide insight into magmatic arc basement, mafic magmatism and structure of the Eastern Ross Sea Rift flank: Tectonophysics, **347**, 139-165.

FitzGerald, D., Reid, A., McInerney, P., 2004. New discrimination techniques for Euler deconvolution: Computers & Geosciences, **30**, 461-469.

Gohl, K., Denk, A., Eagles, G., Wobbe, F., 2013. Deciphering tectonic phases of the Amundsen Sea Embayment shelf, West Antarctica, from a magnetic anomaly grid: Tectonophysics, **585**, 113-123.

Gopal, K.G. 2016. Interpretation of gravity data using 3D Euler deconvolution, tilt angle, horizontal tilt angle and source edge approximation of the North-West Himalaya: Acta Geophysica, **64**, 1112-1138.

Guoqing, M., 2014. The application of extended Euler deconvolution method in the interpretation of potential field data: Journal of Applied Geophysics, **107**, 188-194.

Hadhemi, B., Fatma, H., Ali, K., Mohamed, G., 2016. Subsurface structure of Teboursouk and El Krib plains (dome zone, northern Tunisia) by gravity analysis: Journal of South African Earth Sciences, **119**, 78-93.

Harrouchi, L., Hamoudi, M., Bendaoud, A., Beguiret, L., 2016. Application of 3D Euler deconvolution and improved tilt angle to the aeromagnetic data of In Ouzzal terrane, western Hoggar, Algeria: Arabian Journal of Geosciences, **9**,:508. https://doi.org/10.1007/s12517-016-2536-1.

Hsu, S.-K., 2002. Imaging magnetic sources using Euler's equation: Geophysical Prospecting, **50**, 15-25.

Ibraheem, I.M., Elawadi, E.A., El-Qady, G.M., 2018. Structural interpretation of aeromagnetic data for the Wadi El Natrun area, northwestern desert, Egypt: Journal of South African Earth Sciences, **139**, 14-25.

Jammes, S., Tiberi, C., Manatschal, G., 2010. 3D architecture of a complex transcurrent rift system: The example of the Bay of Biscay-Western Pyrenees: Tectonophysics, **489**, 210-226.

Jordan, T.A., Feraccioli, F., Ross, N., Corr, H.F.J., Leat, P.T., Bingham, R.G., Rippin, D.M., Brocq, A., Siegert, M.J., 2013. Inland extent of the Weddell Sea Rift imaged by new aerogeophysical data: Tectonophysics, **585**, 137-160.

Khalil, M.H., 2016. Subsurface faults detection based on magnetic anomalies investigation: A field example at Taba protectorate, South Sinai: Journal of Applied Geophysics, **131**, 123-132.

MacLeod, I.N., Vierra, S., Chaves, A.C., 1993. Analytic signal and reduction-to-the-pole in the interpretation of total magnetic field data at low magnetic latitudes. Proceedings of the 3rd International Congress of the Brazilian Geophysical Society, Expanded Abstracts, 830-835.

Martins-Ferreira, M.A.C., Campos, J.E.G., Huelsen, M.G.V., Neri, B.L., 2018. Paleorift structure constrained by gravity and stratigraphic data: The Statherian Araí rift case: Tectonophysics, **738-739**, 64-82.

Mazabraud, Y., Béthoux, N., Deroussi, S., 2005. Characterisation of the seismological pattern in a slowly deforming intraplate region: central and western France: Tectonophysics, **409**, 175-192.

Melo, F.F., Barbosa, V.C.F., 2017. Correct structural index defined by base level estimates in Euler Deconvolution: 15th International Congress of the Brazilian Geophysical Society & EXPOGEF, SBGF, 1086-1091. https://doi.org/10.1190/sbgf2017-212.

Melo, F.F., Barbosa, V.C.F., 2017. What to expect from Euler Deconvolution estimates for isolated sources: 15th International Congress of the Brazilian Geophysical Society & EXPOGEF, SBGF, 1092-1097. https://doi.org/10.1190/sbgf2017-213.

Melo, F.F., Barbosa, V.C.F., Uieda, L., Oliveira Jr., V., Silva, J.B.C., 2013. Estimating the nature and the horizontal and vertical positions of 3D magnetic sources using Euler deconvolution: Geophysics, **78**, 87-98.

Mieth, M., Jokat, W., 2014. Banded iron formation (?) at Grunehogna Craton, East Antarctica-constraints from aeromagnetic data: Precambrian Research, **250**, 143-150.

Mikhailov, V., Galdeano, A., Diament, M, Gvishiani, A., Agayan, S., Bogoutdinov, S., Graeva, E., Sailhac, P., 2003. Application of artificial intelligence for Euler solutions clustering: Geophysics, **68**, 168-180.

Minelli, L., Vecchio, A., Speranza, F., Nicolosi, I., Caracciolo, F.A., Chiappini, S., Carluccio, R., Chiappini, M., 2016. Aeromagnetic investigation of southern Calabria and the Messina Straits (Italy): Tracking seismogenic sources of 1783 and 1908 earthquakes: Journal of Geophysical of Research, **121**, 1297-1315.

Moghtaderi, N., Dehkordi, B.H., Oskooi, B., 2017. Characterization of the Houze-Vali iron ore in the centre of Iran using magnetic gradient tensor data: Bollettino di Geofisica Teorica ed Applicata, **58**, 205-216, doi: 10.4430/bgta0196.

Mushayandebvu, M.F, Driel P.van, Reid, A.B., Fairhead, J.D., 2001. Magnetic source parameters of two-dimensional structures using extended Euler deconvolution: Geophysics, **66**, 814-823.

Mushayandebvu, M.F, Lesur, V., Reid, A.B., Fairhead, J.D., 2004. Grid Euler deconvolution with constraints for 2D structures: Geophysics, **69**, 489-496.

Ndougsa-Mbarga, T., Feumoe, A.N.S., Manguelle-Dicoum, E., Fairhead, J.D., 2012. Aeromagnetic Data Interpretation to Locate Buried Faults in South- East Cameroon: Geophysica, **48**, 49-63.

Okabe, M., 1979. Analytical expressions for gravity anomalies due to homogeneous polyhedral bodies and translations into magnetic anomalies: Geophysics, **44**, 730-741.

Oladunjoye, M.A., Olayinka, A.I., Alaba, M.; Adabanija, M.A., 2016. Interpretation of high resolution aeromagnetic data for lineaments study and occurrence of banded iron formation in Ogbomoso area, Southwestern Nigeria: Journal of African Earth Sciences, **114**, 43-56.

Olasunkanmi, N.K., Bamigboye, O.S., Aina, A., 2017. Exploration for iron ore in Agbado-Okudu, Kogi State, Nigeria: Arabian Journal of Geosciences, **10**:541. https://doi.org/10.1007/s12517-017-3250-3.

Oliveira, R.G., Medeiros, W.E., 2018, Deep crustal framework of the Borborema Province, NE Brazil, derived from gravity and magnetic data: Precambrian Research, **315**, 45-65. https://doi.org/10.1016/j.precamres.2018.07.004.

Oruç, B., Keskinsezer, A., 2008. Detection of causative bodies by normalized full gradient of aeromagnetic anomalies from east Marmara region, NW Turkey: Journal of Applied Geophysics, **65**, 39-49.

Oruç, B., Selim, B.B., 2011. Interpretation of magnetic data in the Sinop area of Mid Black Sea, Turkey, using tilt derivative, Euler deconvolution, and discrete wavelet transform: Journal of Applied Geophysics, **74**, 194-204.

Osinowo, O.O., Akanji, A.O., Olayinka, A.I., 2014. Application of high resolution aeromagnetic data for basement topography mapping of Siluko and environs, southwestern Nigeria: Journal of South African Earth Sciences, **99**, 637-651.

Pilkington, M., Saltus, R.W., 2009. The Mackenzie River magnetic anomaly, Yukon and Northwest Territories, Canada - Evidence for Early Proterozoic magmatic arc crust at the edge of the North American craton: Tectonophysics, **478**, 78-86.

Rabii, F., Jallouli, C., Mickus, K., Soumaya, A., Rebai, N., Ayed, N.B., 2018. New insights on structures and active faults in northeastern Tunisia (Utica-Mateur region) from a gravity analysis: geodynamic implications: Journal of South African Earth Sciences, **147**, 54-67.

Reeh, G., Aifa, T., 2008. Age of the source of the Jarrafa gravity and magnetic anomalies offshore Libya and its geodynamic implications: Journal of Geodynamics, **45**, 217-233.

Reid, A.B., 2003. Euler magnetic structural index of a thin-bed fault: Geophysics, **68**, 1255-1256.

Reid, A.B.; Allsop, J.M. Granser; H., Millett, A.J., Somerton, I.W., 1990. Magnetic interpretation in three dimensions using Euler deconvolution: Geophysics, **55**, 80-91.

Reid, A.B., FitzGerald, D., McInerny, P., 2003. Euler deconvolution of gravity data. SEG Technical Program Expanded Abstracts, 80-583. https://doi.org/10.1190/1.1817993.

Rocha, L.G.M., Pires, A.C.B., Carmelo, A.C., Filho, J.O.A., 2014. Geophysical characterization of the azimuth 125° lineament with aeromagnetic data: Contributions to the geology of central Brazil: Precambrian Research, **249**, 273-287.

Rodrigues, R.S., Castro, D.L., Reis Jr., J.A., 2014. Characterization of the Potiguar rift structure based on Euler deconvolution: Brazilian Journal of Geophysics, **32**, 109-121.

Sanchez-Rojas, J., Palma, M., 2014. Crustal density structure in northwestern South America derived from analysis and 3-D modeling of gravity and seismicity data: Tectonophysics, **634**, 97-115.

Silva, B.C.J., 1986. Reduction to the pole as an inverse problem and its application to low latitude anomalies: Geophysics, **51**, 369-382.

Silva, J.B.C., Barbosa, V.C.F., Medeiros, W.E., 2001. Scattering, symmetry, and bias analysis of source-position estimates in Euler deconvolution and its practical implications: Geophysics, **66**, 1149-1156.

Sridhar, M., Babu, V.R., Markandeyulu, A., Raju, B.V.S.N., Chaturvedi, A.K., Roy, M.K., 2017. A reassessment of the archean-mesoproterozoic tectonic development of the southeastern Chhattisgarh Basin, Central India through detailed aeromagnetic analysis: Tectonophysics, **712-713**, 289-302.

Thompson, D.T., 1982. EULDPH: A new technique for making depth estimates from magnetic data: Geophysics, **47**, 31–37.

Uchôa Filho, E.A., Freitas, M.S., 2017. Complexos Santa Filomena e Paulistana. Teresina, CPRM. Mapa colorido 163,99 x 89,99 cm. Escala 1:100.000. Integração geológica e de recursos minerais das faixas marginais da borda norte-noroeste do

Cráton São Francisco (Empreendimento Áreas de Relevante Interesse Mineral-ARIM). (available at <geosgb.cprm.gov.br>).

Ugalde, H., Morris, W.A., 2010. Cluster analysis of Euler deconvolution solutions: new filtering techniques and geologic strike determination: Geophysics, **75**, 61-70.

Uieda, L., Oliveira, J.R, V.C., Barbosa, V.C.F., 2014. Geophysical tutorial: Euler deconvolution of potential-field data: The Leading Edge, **33**, 448-450.

Wang, J., Meng, X., Li, F., 2017. New improvements for lineaments study of gravity data with improved Euler inversion and phase congruency of the field data: Journal of Applied Geophysics, **136**, 326-334.

Weihermann, J.D., Ferreira, F.J.F., Oliveira, S.P., Cury, L.F., Souza, J., 2018. Magnetic interpretation of the Paranaguá Terrane, southern Brazil by signum transform: Journal of Applied Geophysics, **154**, 116-127.

Werner, S.C., Torsvik, T.H., 2010. Downsizing the Mjølnir impact structure, Barents Sea, Norway: Tectonophysics, **483**, 191-202.

Widiwijayanti, C., Tiberi, C., Deplus, C., Diament, M., Mikhailov, V., Louat, R., 2004. Geodynamic evolution of the northern Molucca Sea area (Eastern Indonesia) constrained by 3-D gravity field inversion: Tectonophysics, **386**, 203-222.

Zhang, C., Mushayandebvu, M.F., Reid, A.B., Fairhead, J.D., Odegard, M.E., 2000, Euler deconvolution of gravity tensor gradient data: Geophysics, **65**, 512-520.

Zhang, J., Zhao, G., Shen, W., Li, S., Sun, M., 2015. Aeromagnetic study of the Hengshan-Wutai-Fuping region: Unraveling a crustal profile of the Paleoproterozoic Trans-North China Orogen: Tectonophysics, **662**, 208-218.
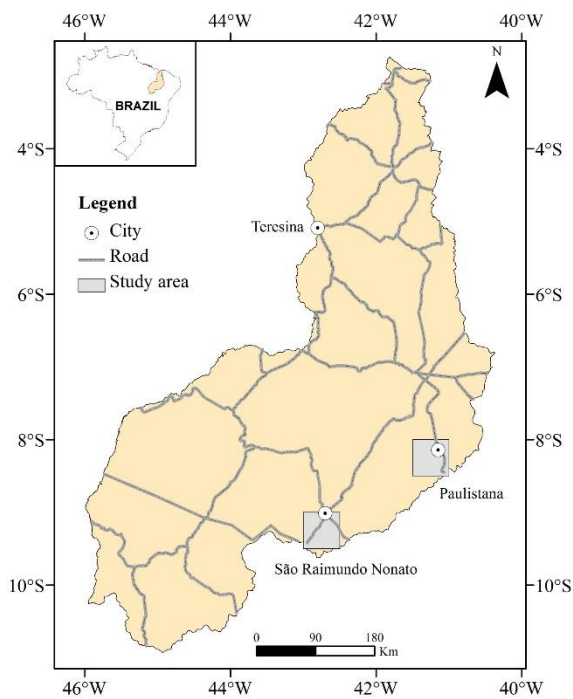
Figure 1- Location map of the study areas in Piauí state, Brazil.
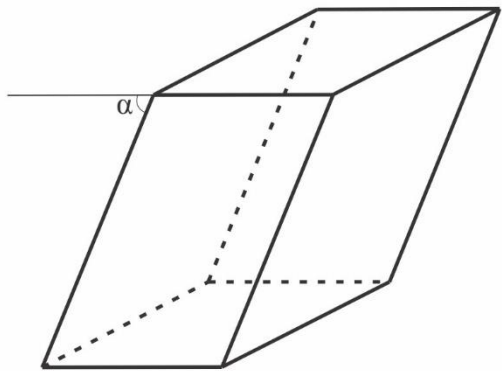
Figure 2- Oblique prism employed in the second criterion (Volume-filtering) of acceptance of the ED solutions. The solutions which are located outside the given prism are discarded (see example in Figures 5b and 5c). The top and bottom faces of the prism are parallel to the Earth's surface and might be rectangles or rhombuses. The prism dimensions and dip (angle α) are inferred from the visual analysis of both the ED solution cluster and the reduced-to-the-pole anomaly.
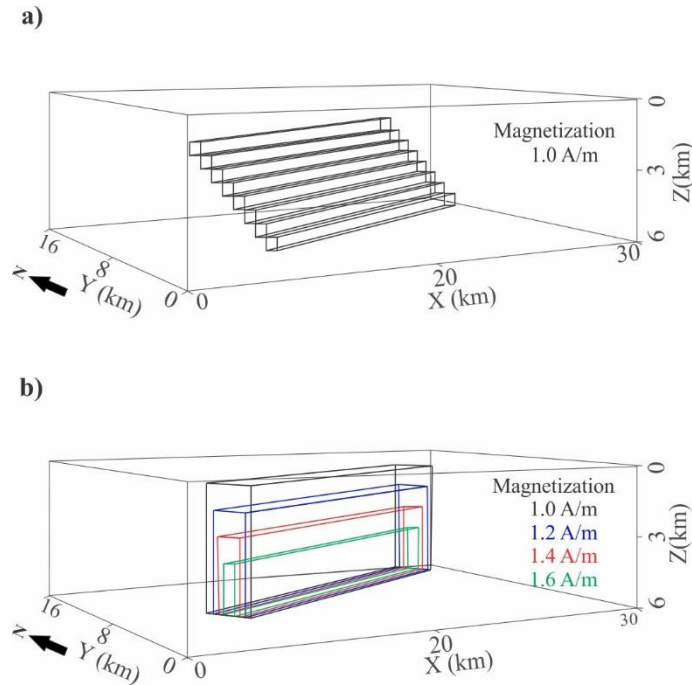
Figure 3- Anomalous synthetic bodies A (a) and B (b). Body A has uniform contrast of magnetization (1.0 A/m) but rough delimiting interfaces. On the other hand, Body B has smooth interfaces but strong internal contrasts of magnetization intensity. In (b) the magnetization intensity inside each prism is cumulative. As example, the intensity contrasts relative to the surrounding medium is 1.0 A/m and 5.2 A/m for the outermost (in black) and innermost (in green) prisms, respectively.
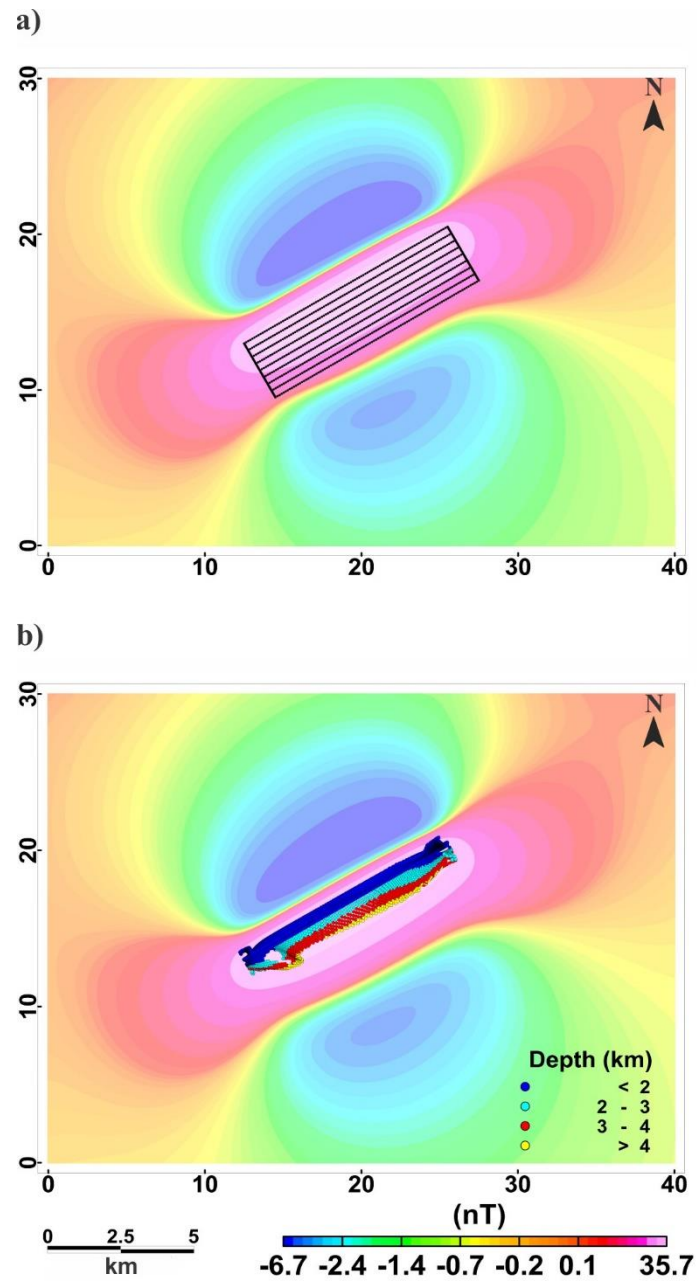
Figure 4- Body A: Reduced-to-the-pole anomaly and the projections on the Earth's surface of the body edges (a) and ED solutions (b). ED parameters are shown in Table 1. The color bar for the field intensity is the same for maps (a) and (b).
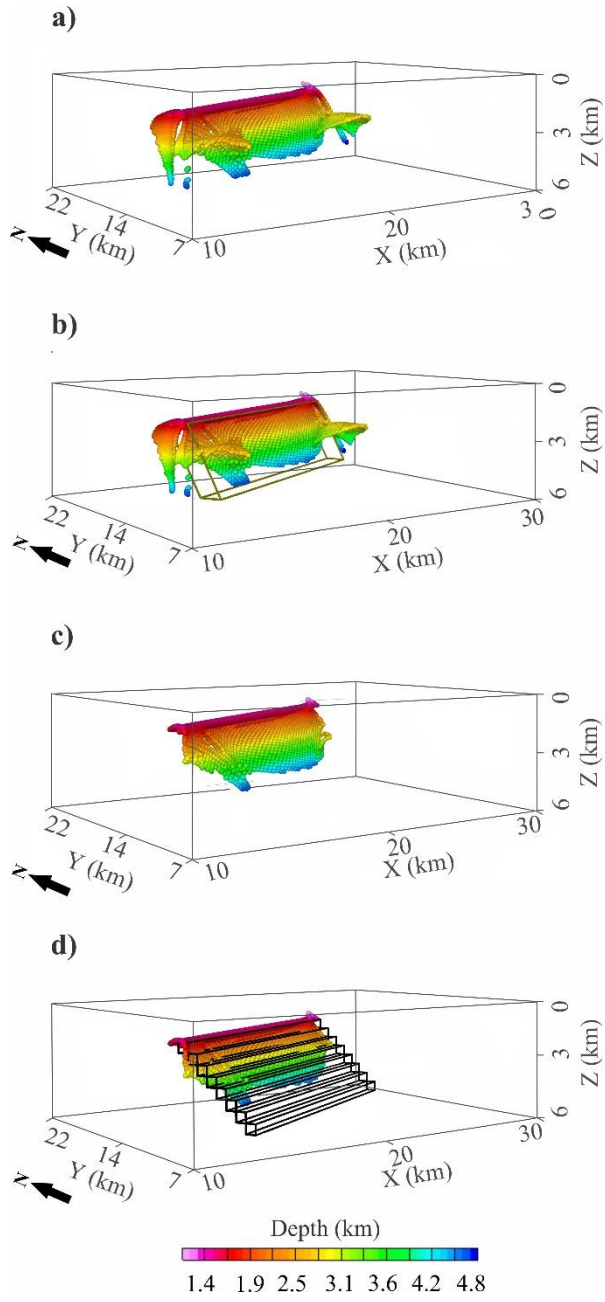
Figure 5- Body A: 3D views of the ED solutions obtained with SI = 1. After applying only the Depth-filtering criterion (a), the same in a joint view with the prism employed for the Volume-filtering criterion (b), after applying both Depth- and Volume-filtering criteria (c), and the same in a joint view with the source (d). The color bar for the depth of the ED solutions is the same for all cases.
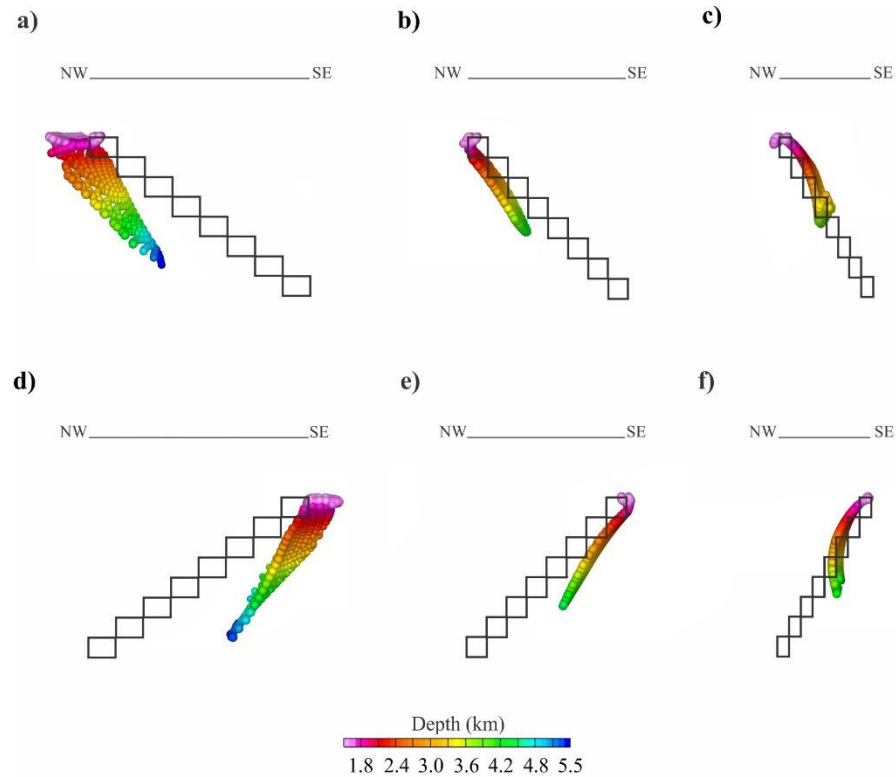
Figure 6- Body A: Projections of the ED solutions on the vertical section transversal to the body strike and passing through its center. Different cases of body dip are shown to evidence the discrepancy between the body dip and the dip associated with the ED cluster of solutions. Dip angles of 36° to SE, 45° to SE (b, the same as in Figure 5d), 60° to SE (c), 36° to NW (d), 45° to NW (e), and 60° to NW (f). The color bar for the depth of the ED solutions is the same for all cases.
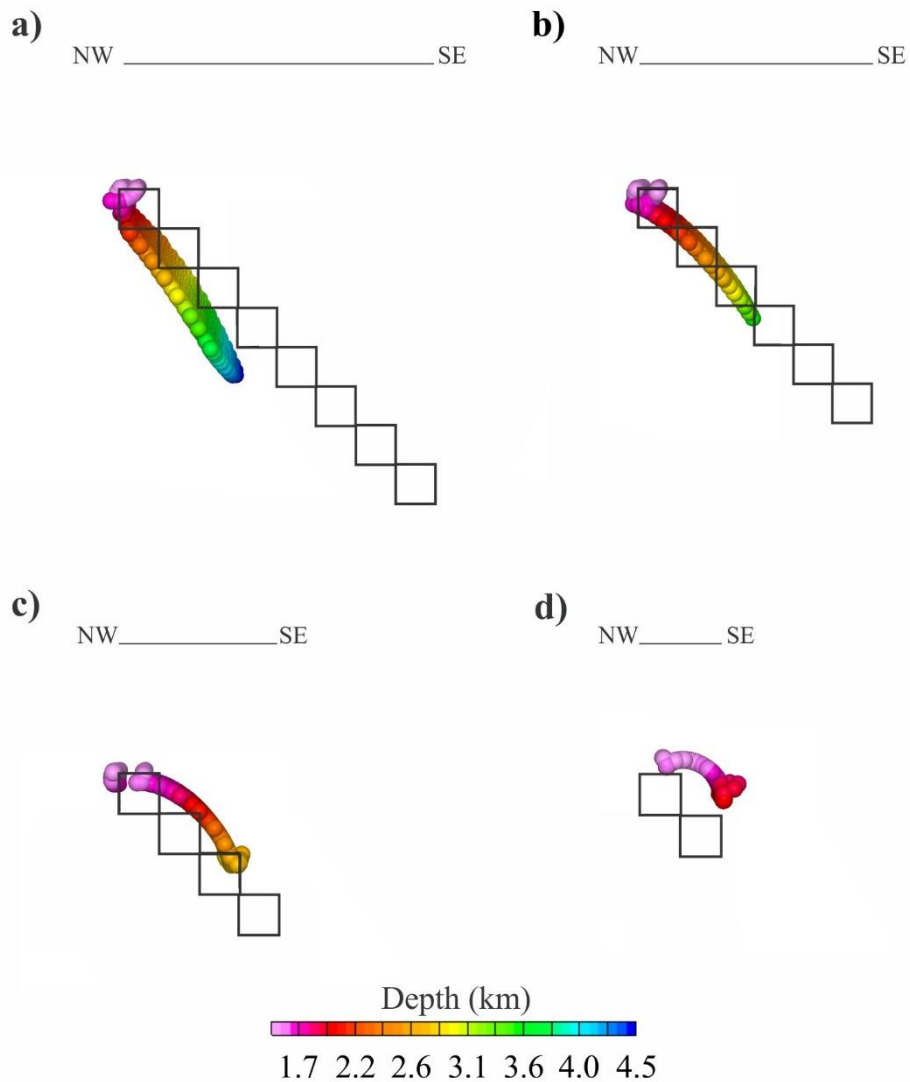
Figure 7- Body A: Projections of the ED solutions on the vertical section transversal to the body strike and passing through its center. In (a), all the stairs (that is, the horizontal prims) composing Body A are maintained (so (a) case is the same as in Figure 6b), but from (b) to (d), the stairs were gradually removed, one pair at a time, starting with the deepest pair (b). The color bar for the depth of the ED solutions is the same for all cases.
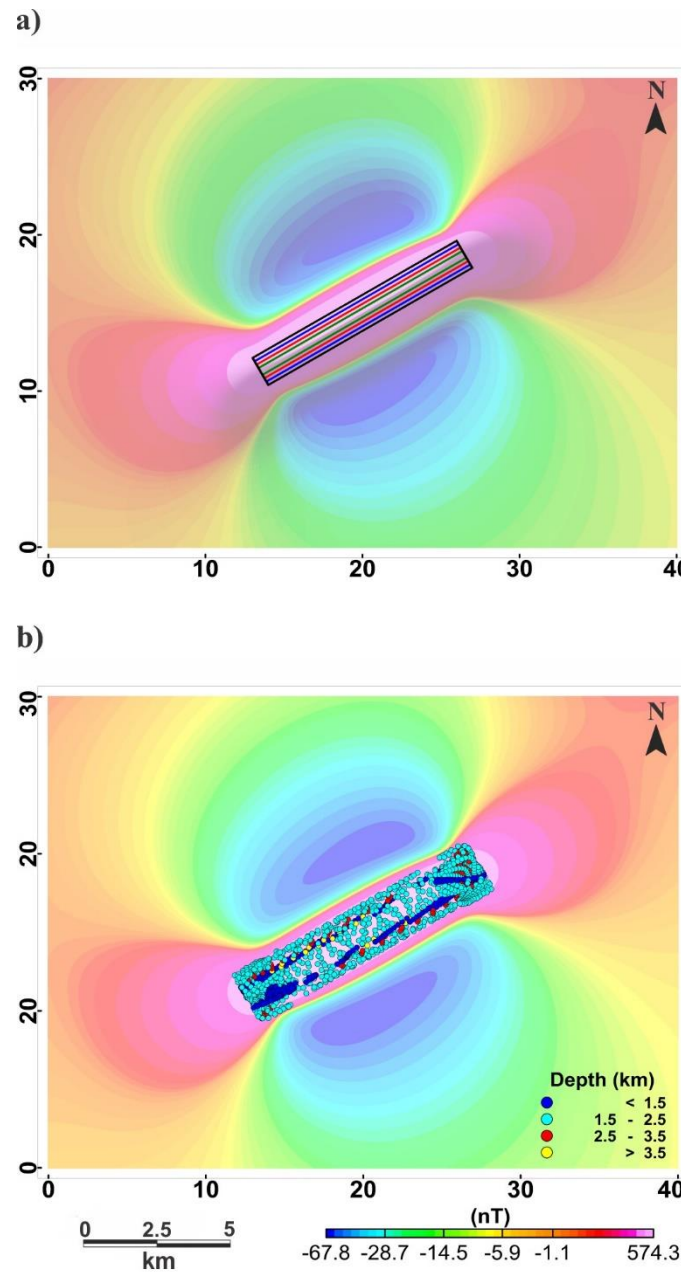
Figure 8- Body B: Reduced-to-the-pole anomaly and the projections on the Earth's surface of the body edges (a) and ED solutions obtained with SI = 3 (b). The colors used for the body edges in (a) are the same used in Figure 3b. ED parameters are shown in Table 1. The color bar for the field intensity is the same for maps (a) and (b).
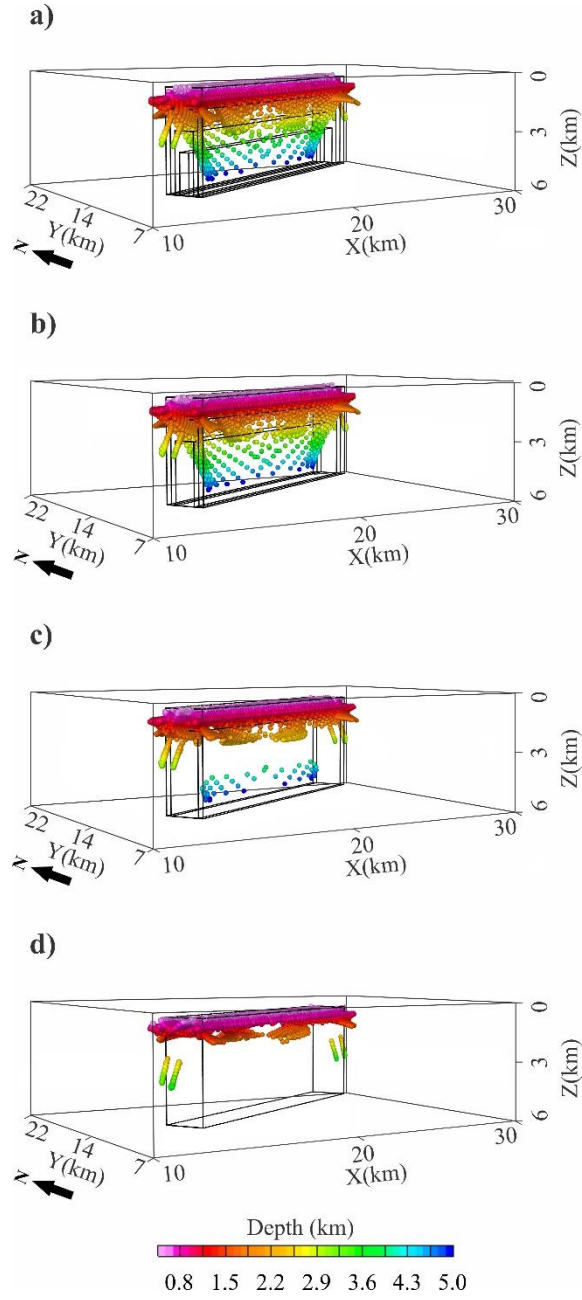
Figure 9- Body B: 3D views of the ED solutions obtained with SI = 1. In (a), all the internal contrasts of magnetization shown in Figure 3b are maintained, but from (b) to (d), these contrasts were gradually removed, one by one, starting in (b), where just the innermost prism was removed, and ending in (d), where just the outmost external prism remains. The color bar for the depth of the ED solutions is the same for all cases.
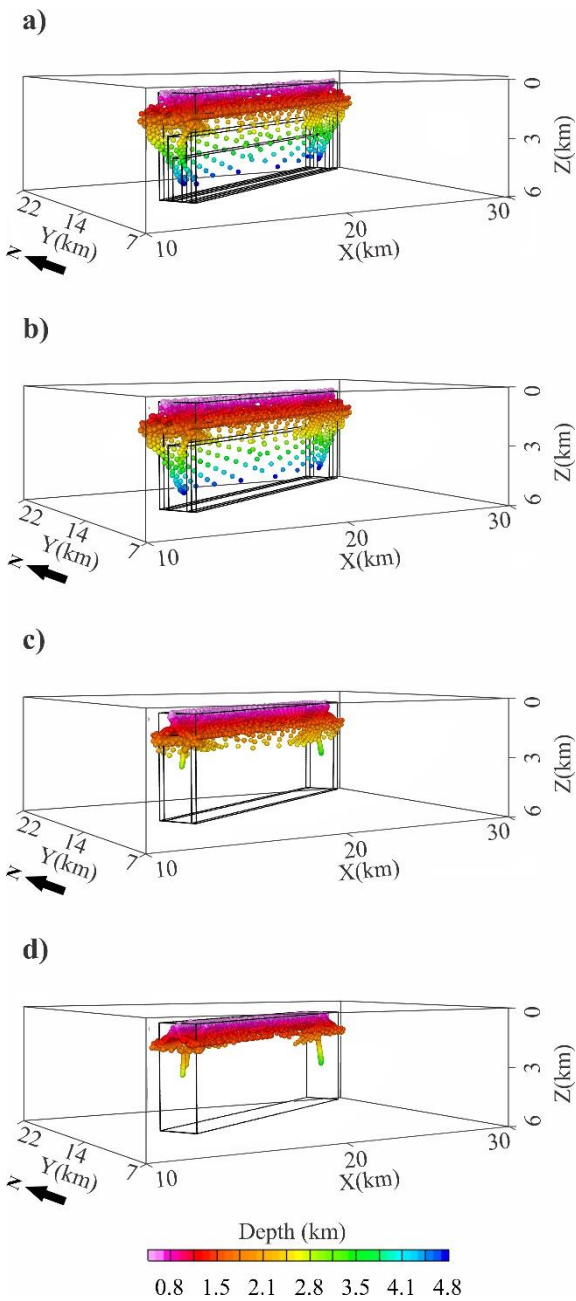
Figure 10- Body B: The same is in Figure 9 but now using SI = 2. The color bar for the depth of the ED solutions is the same for all cases.
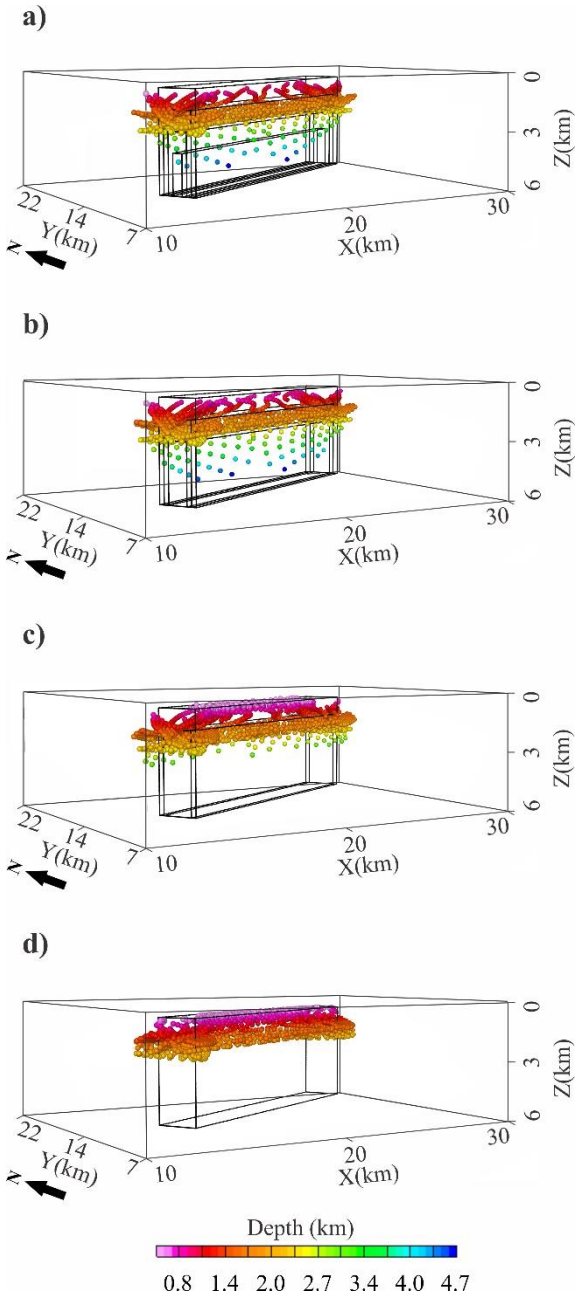
Figure 11- Body B: The same is in Figure 9 but now using SI = 3. The color bar for the depth of the ED solutions is the same for all cases.
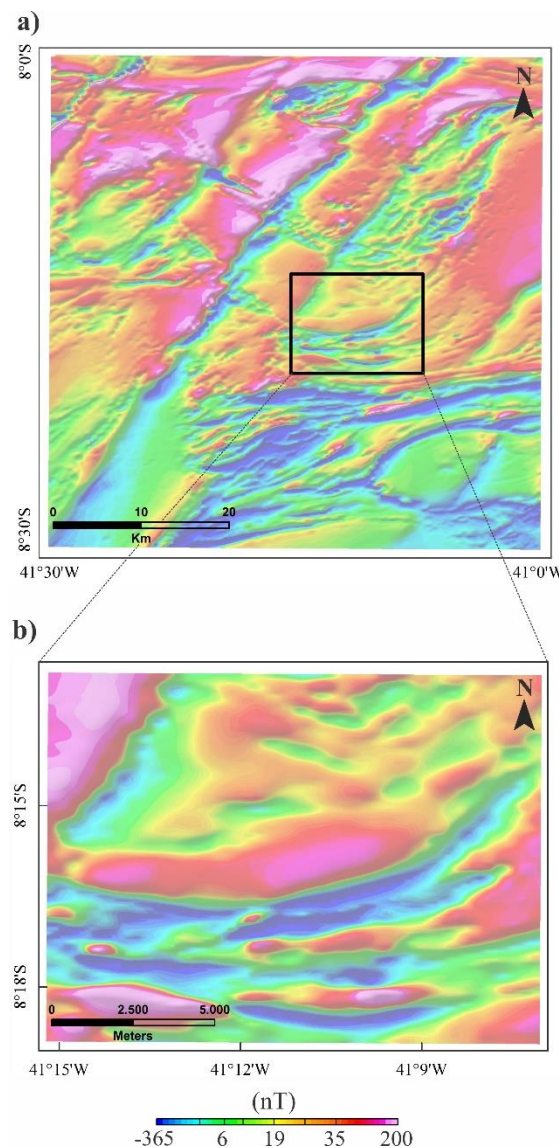
Figure 12- Paulistana study area: Maps of aeromagnetic anomalies in regional (a) and local (b) views. The study area is located in Piauí state, Brazil (Figure 1). The geomagnetic field has inclination and declination equal to approximately -23° and -22°, respectively. Maps (a) and (b) are on the same scales as the geologic maps shown in Figures 13a and 13b, respectively. The color bar for the field intensity is the same for maps (a) and (b). Comparing magnetic and geologic maps one can verify that the curved-shaped thrust zone is associated with a magnetic anomaly.

a)

b)

PHANEROZOIC
- Phanerozoic covers

NEOPROTEROZOIC
- Post-orogenic suites
- Synorogenic suites
- Meta-volcano-sedimentary sequence
- Pre-orogenic suite

PALEO-NEO ARCHEAN
- Basement

Structures

Anticlinal fold	Thrust zone	Fracture
Dike	Transcurrent dextral fault	Structural lineament
	Transcurrent sinistral fault	Shear zone
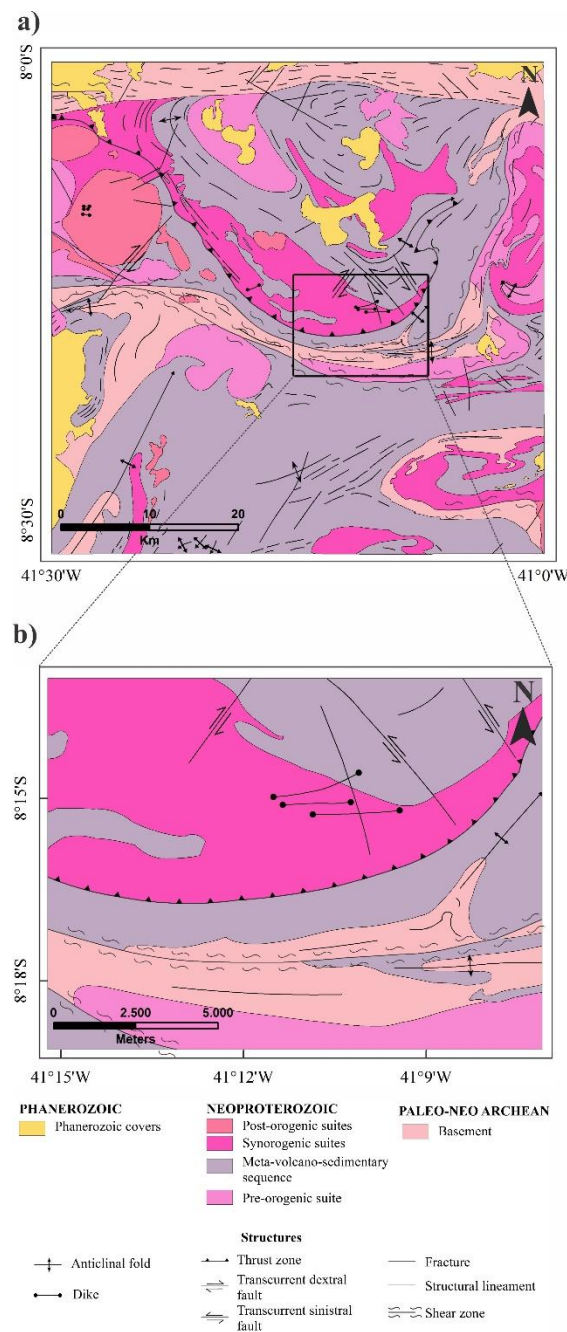
Figure 13- Paulistana study area: Geologic maps in regional (a) and local (b) views. Adapted from Uchôa Filho and Freitas (2017).
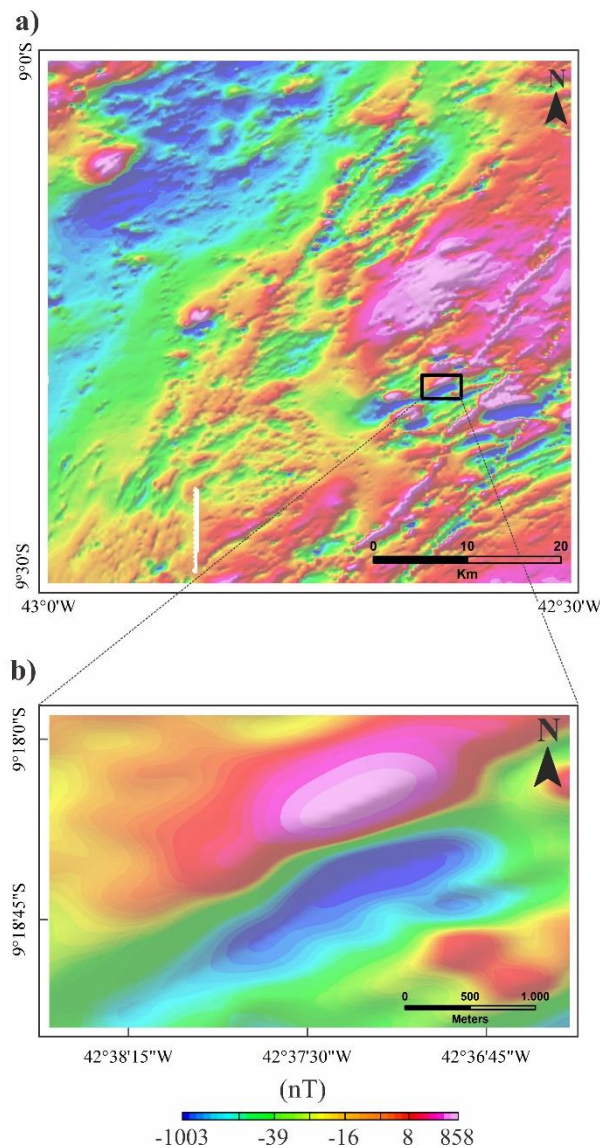
Figure 14- São Raimundo Nonato study area: Maps of aeromagnetic anomalies in regional (a) and local (b) views. The study area is located in Piauí state, Brazil (Figure 1). The geomagnetic field has inclination and declination equal to approximately -23° and -22°, respectively. Maps (a) and (b) are on the same scales as the geologic maps shown in Figures 15a and 15b, respectively. The color bar for the field intensity is the same for maps (a) and (b). Comparing magnetic and geologic maps one can verify that strong magnetic anomalies might occur in association with a Neoarchean meta-volcano-sedimentary sequence.
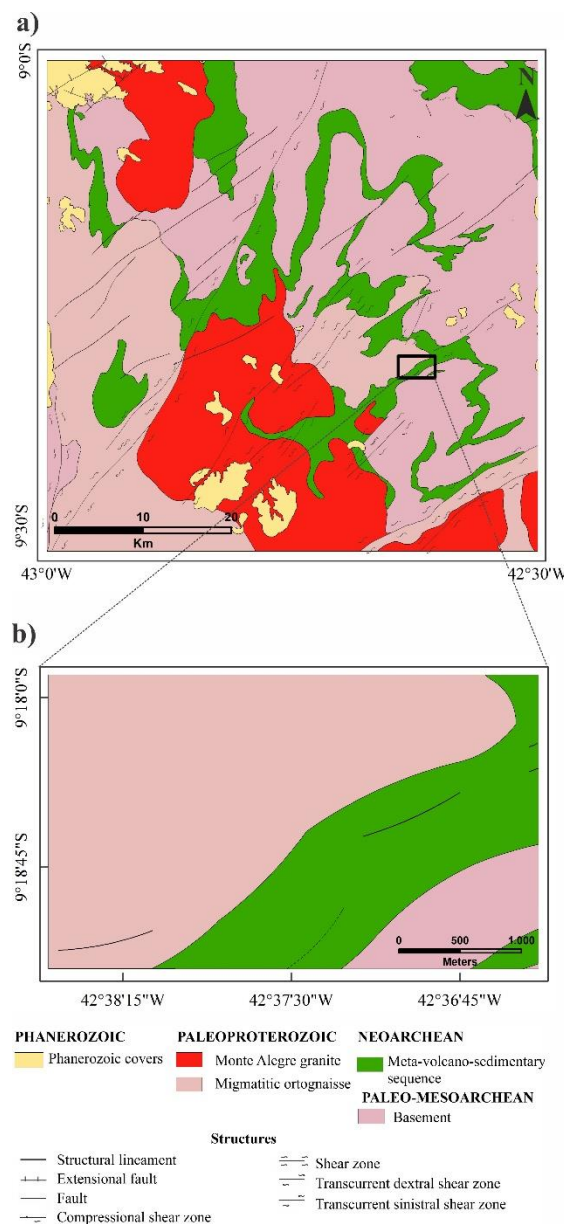
Figure 15- São Raimundo Nonato study area: Geologic maps in regional (a) and local (b) views. Adapted from Augusto and Santos (2014).
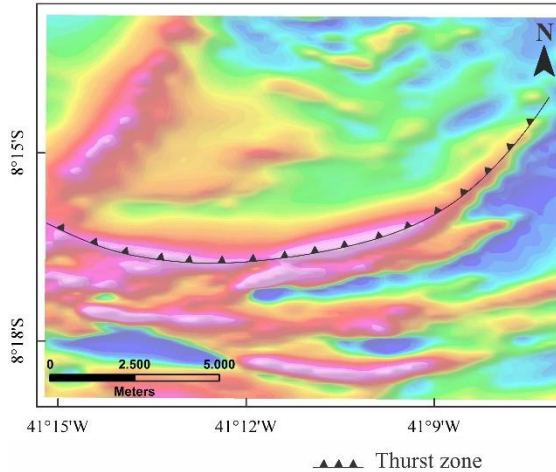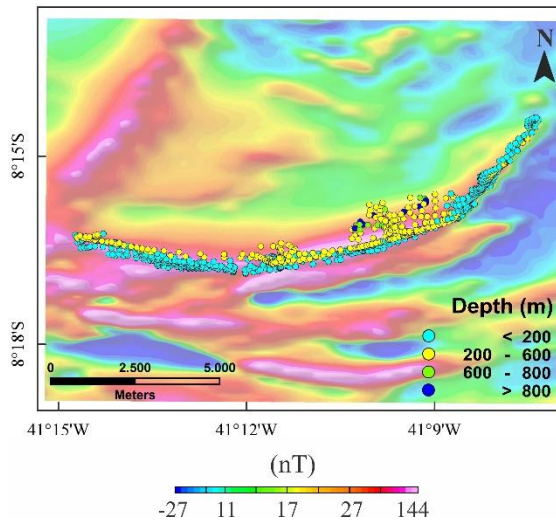
Figure 16- Paulistana study area: Reduced-to-the-pole version of the magnetic anomaly shown in Figure 12b superposed to the outcropping thrust zone (a) and to the ED solution cluster obtained with SI = 1 (b). ED parameters are shown in Table 1. The color bar for the field intensity is the same for maps (a) and (b).
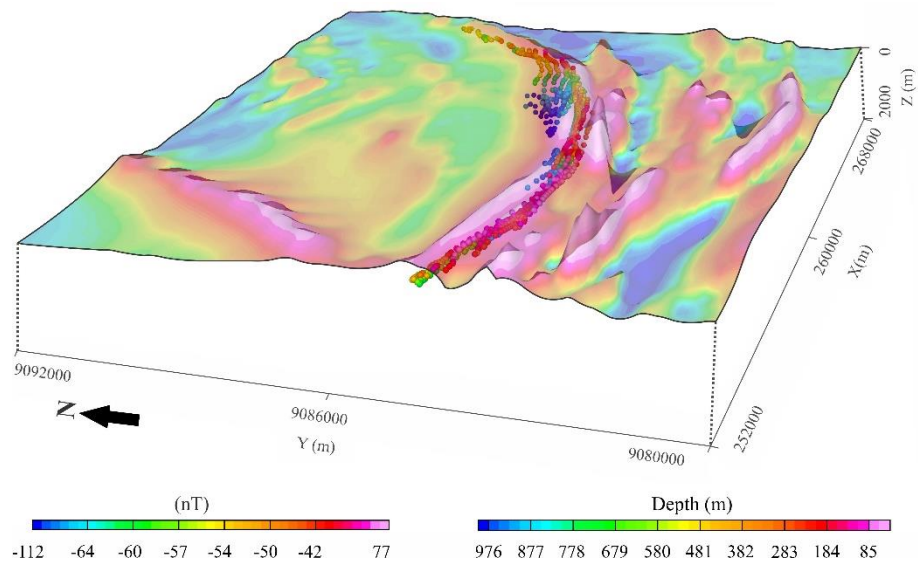
Figure 17- Paulistana study area: Joint 3D view of the reduced-to-the-pole magnetic anomaly and ED solution cluster. The variation in the dip direction of the ED solutions can be seen.
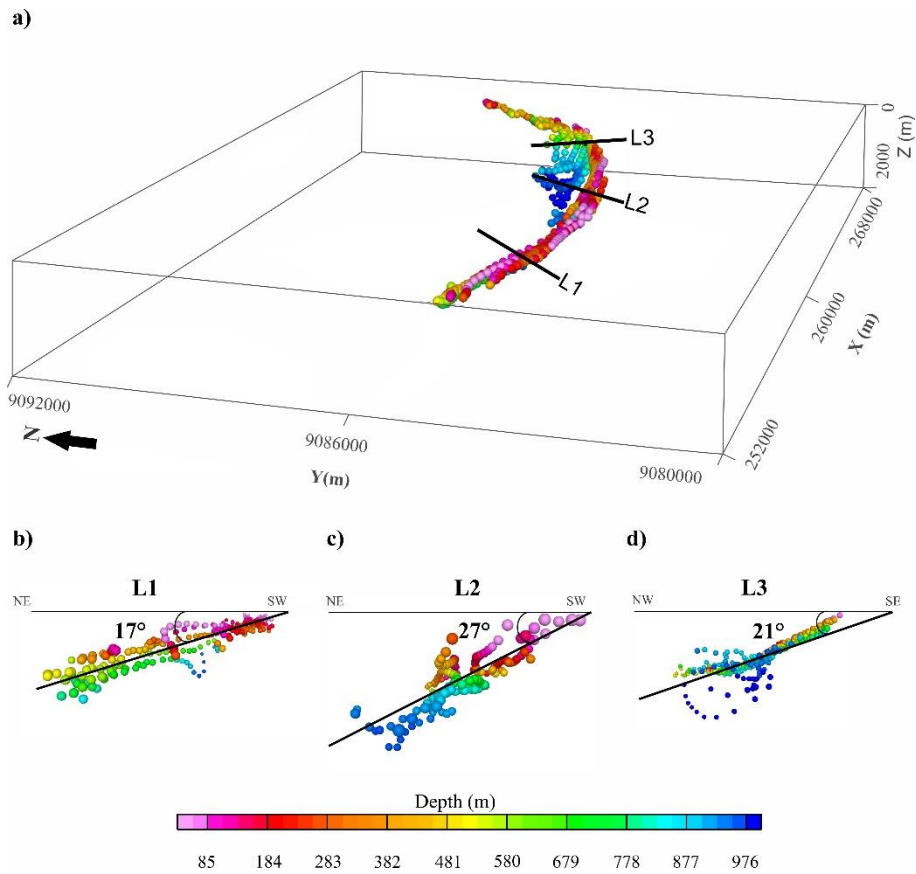
Figure 18- Paulistana study area: 3D view of the ED solution cluster (a) and projections on the vertical sections transversal to the thrust zone of the ED solution subsets which are near the profiles L1 (b), L2 (c), and L3 (c). The color bar for the depth of the ED solutions is the same for all views. From (b) to (d), the shown lines and angles highlight the local mean dip of the solution cluster.
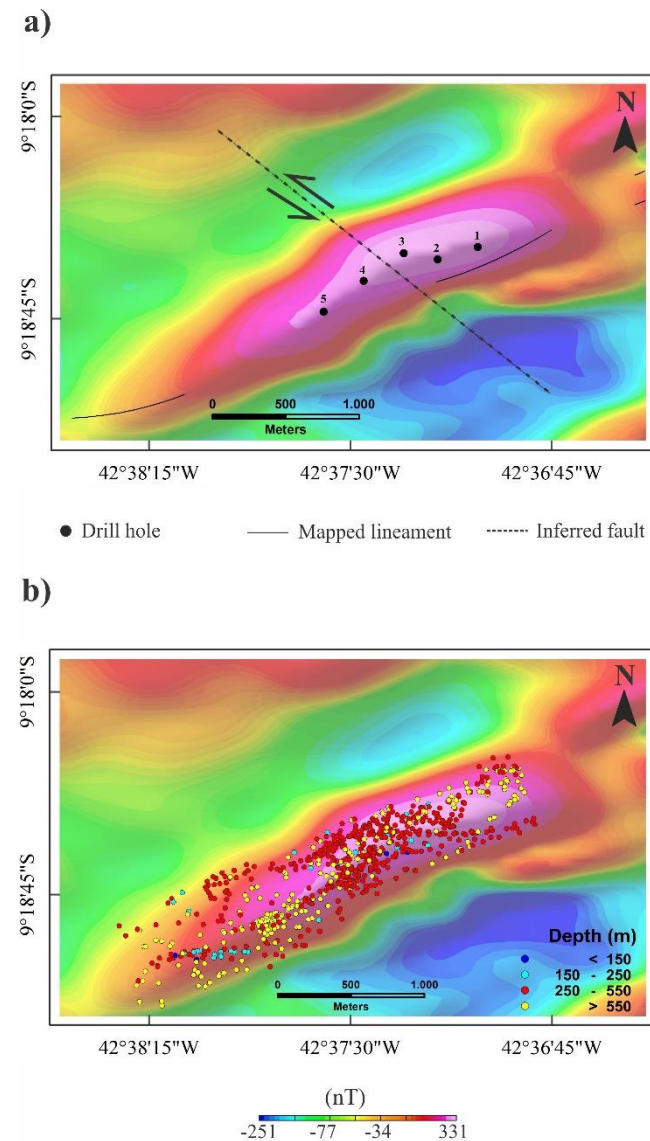
Figure 19- São Raimundo Nonato study area: Reduced-to-the-pole version of the magnetic anomaly shown in Figure 14b superposed to the known (Augusto and Santos, 2014) or inferred geological information (a) and to the ED solution cluster obtained with SI = 3 (b). Information about the drill holes are given in Cordani (2011). ED parameters are shown in Table 1. The color bar for the field intensity is the same for maps (a) and (b).
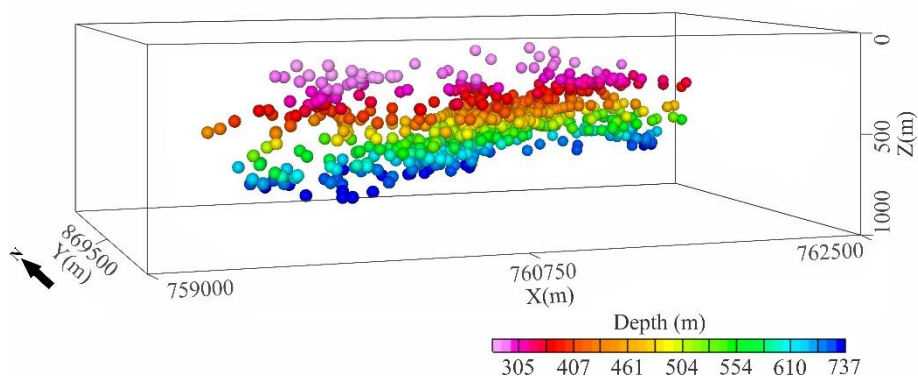
Figure 20- São Raimundo Nonato study area: 3D view of the ED solution cluster.
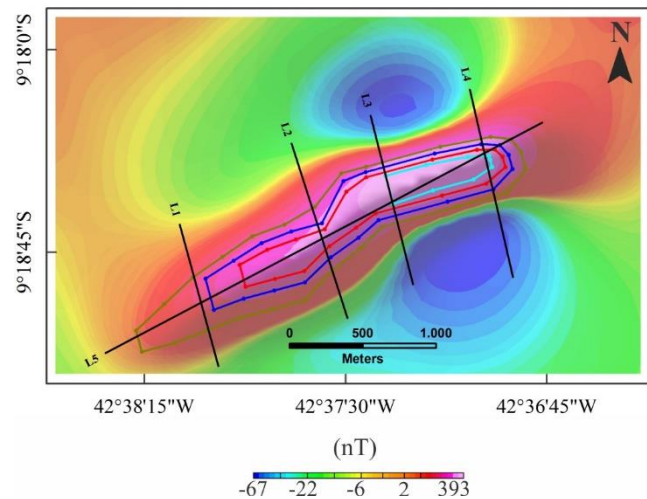
Figure 21- São Raimundo Nonato study area: Reduced-to-the-pole version of the synthetic magnetic anomaly resulting from a trial-and-error 3D modeling of the field anomaly shown in Figure 19a. The projections on the Earth's surface of the edges of the modeled magnetization distribution (Figure 22a) and the location of five profiles are also shown. The colors used for the body edges are the same used in Figure 22a.
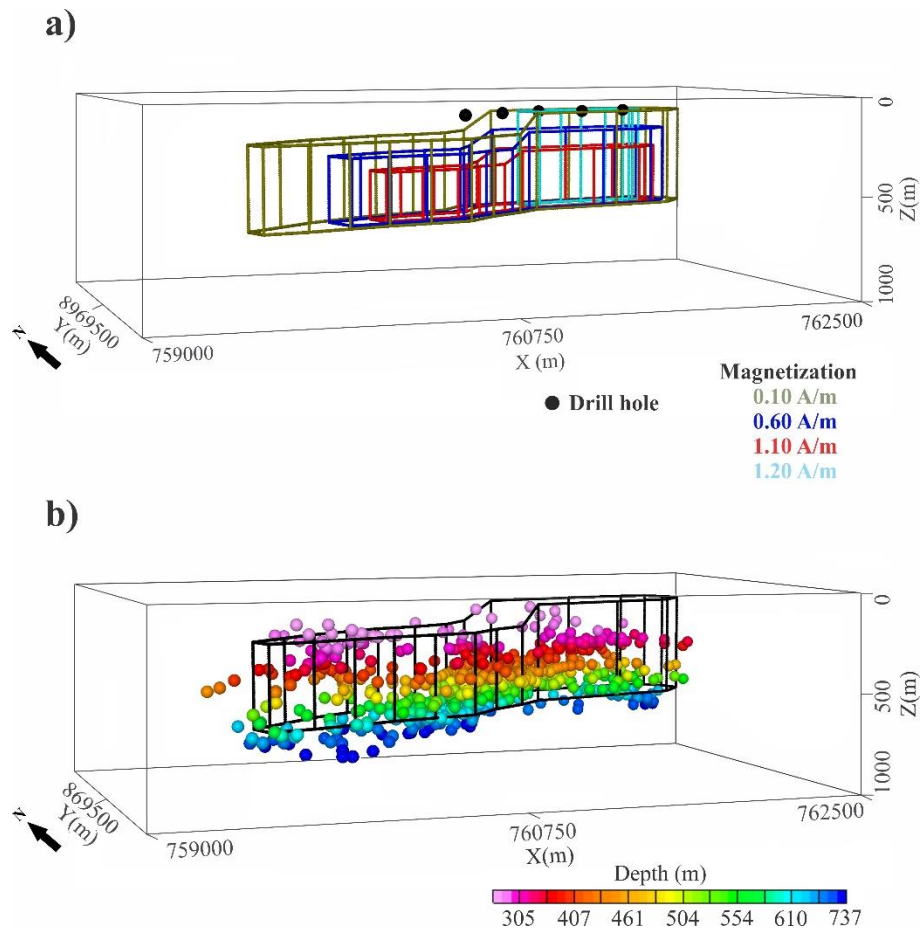
Figure 22- São Raimundo Nonato study area: 3D views of the modeled magnetization distribution. In (a), all internal intensity contrasts are shown, besides the drill hole positions. As in the synthetic Body B, the magnetization intensity inside each prism is cumulative. In (b), only the outmost external body is shown with the ED solution cluster obtained with the field anomaly (that is, the same solution cluster shown in Figure 20).
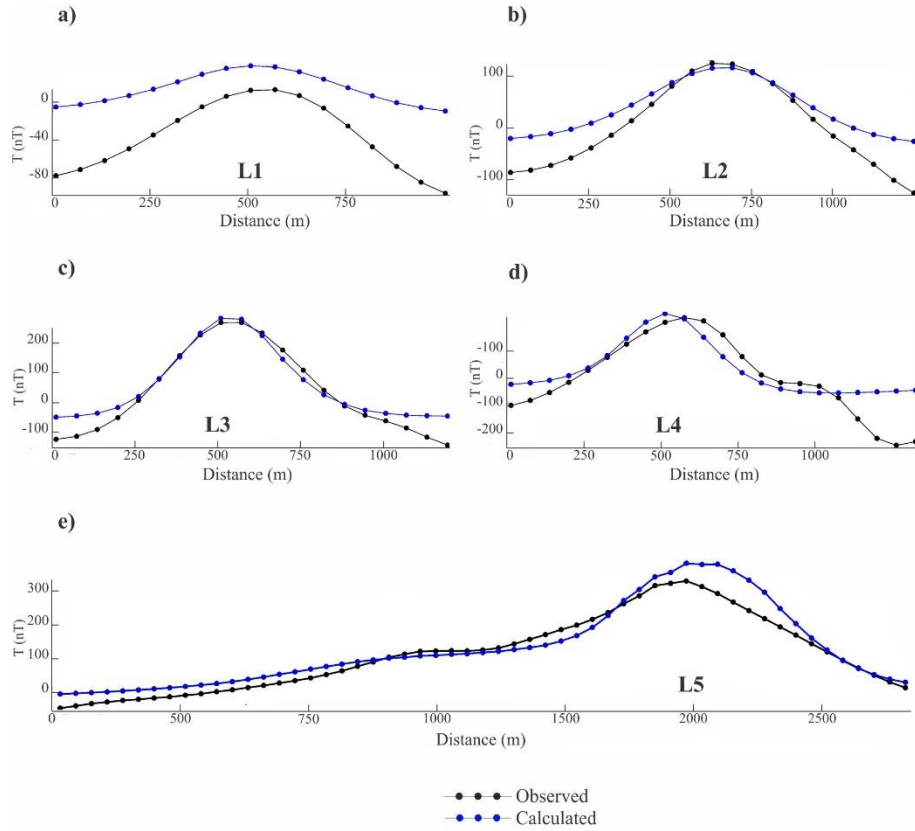
Figure 23- São Raimundo Nonato study area: Comparison between field and synthetic (or calculated) magnetic anomalies along profiles L1 to L5. The synthetic magnetic anomaly is due to the magnetization distribution (Figure 22a), resulting from a trial-and-error 3D modeling of the field anomaly (Figure 19a). The location of five profiles are shown in Figure 21.
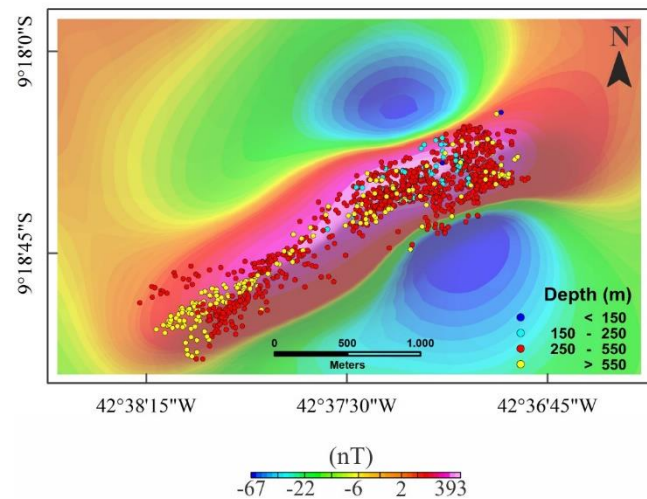
Figure 24- São Raimundo Nonato study area: Synthetic magnetic anomaly resulted from the 3D trial-and-error modeling (also shown in Figure 21) superposed to the ED solution cluster from it obtained using SI = 3. ED parameters are shown in Table 1.
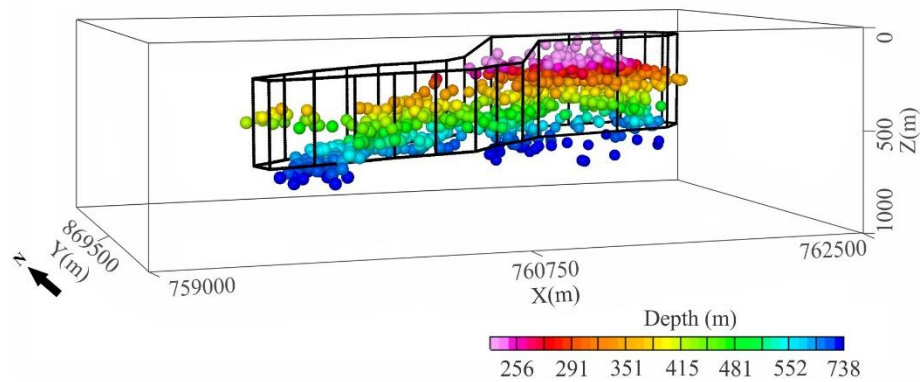
Figure 25- São Raimundo Nonato study area: 3D view the outmost external body resulting from the trial-and-error modeling (Figure 22a) with the ED solution cluster obtained with the synthetic magnetic anomaly (that is, the same solution cluster shown in Figure 24).
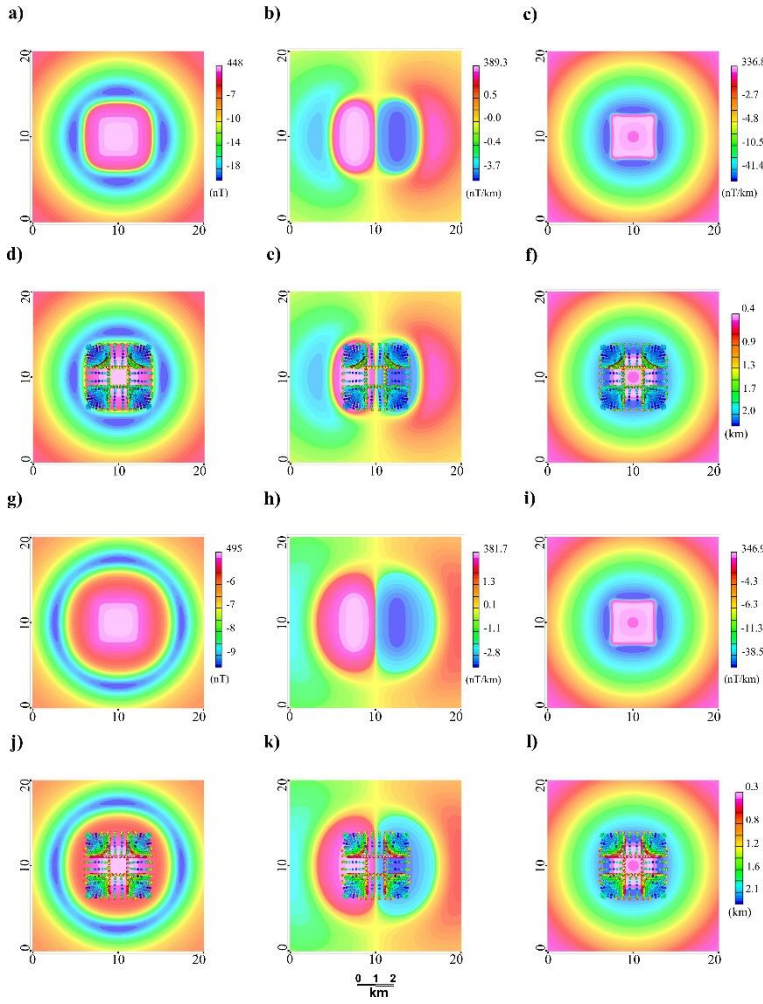
Figure 26- Panel of results showing the effects of doubling the thickness of a vertical prism in its magnetic anomaly (a and g), *x*-component of $\vec{\nabla}T$ (b and h), and *z*-component of $\vec{\nabla}T$ (e and i). The vertical prism generating anomalies (a) to (c) has dimensions 5 x 5 x 5 km^3 whilst the one generating anomalies (g) to (i) has dimensions 5 x 5 x 10 km^3. The induced magnetization (1.0 A/m) and the depth to the upper face (0,5 km) are the same for both prisms. ED solutions obtained in each case are superposed on the three types of anomalies in figures (d) to (f) (thinner prism) and in figures (j) to (l) (thicker prism). ED parameters are shown in Table 1.

Case/Figure	Cell size (m)	SI	Max. depth tolerance (%)	Window size	Max. distance (km)	Flight height (m)
Body A/Fig. 5d	100	1	5	10	5	0
Body A/Fig. 6b	100	1	15	20	6	0
Body A/Fig. 6c	100	1	5	10	5	0
Body A/Fig. 6d	100	1	5	10	5	0
Body A/Fig. 6e	100	1	10	20	6	0
Body A/Fig. 6f	100	1	5	20	6	0
Body A/Fig. 7b	100	1	5	10	4	0
Body A/Fig. 7c	100	1	5	10	4	0
Body A/Fig. 7d	100	1	5	10	3	0
Body B/Fig. 9a	100	1	5	7	5	0
Body B/Fig. 10a	100	2	5	7	5	0
Body B/Fig. 11a	100	3	5	7	5	0
Paulistana anomaly/Fig. 17	125	1	15	20	-	100
São Raimundo Nonato/Fig. 20	62.5	3	15	6	-	100
São Raimundo Nonato/Fig. 25	62.5	3	15	6	-	100
Vertical prism/ Fig. 26d	100	1	5	10	3	0
Vertical prism/ Fig. 26j	100	1	5	10	3	0

Table 1- Parameters used in the ED for all synthetic and field cases. Each case is identified by both its name and the main figure where the solution cluster is shown.

Internal magnetization contrasts	Figure	SI
With all internal prisms	Fig. 11a	3
Removing just the green prism	Fig. 11b	3
Removing the green and red prisms	Fig. 10c	2
Removing the green, red, and blue prisms	Fig. 10d	2

Table 2- Body B: Best SI values resulting from the criteria of minimizing the variations of either the base level and depth estimates (Melo and Barbosa, 2017a and b) for the magnetic anomalies produced by different cases of Body B. Each case is identified by the subset of prisms which compose the internal contrasts of magnetization and by the main figure where the ED solution cluster is shown. The two criteria suggest the same SI value for each case. However, the suggested SI value changes as the internal contrasts of magnetization are removed.

Referências bibliográficas

___

Akinlalu, A.A., Adelusi, A.O., Olayanju, G.M., Adiat, K.A.N., Omosuyi, G.O., Anifowose, A.Y.B., Akeredolu, B.E., 2018. Aeromagnetic mapping of basement structures and mineralization characterisation of Ilesa Schist Belt, Southwestern Nigeria: Journal of South African Earth Sciences, **138**, 383-391.

Al-Saud, M.M., 2014. The role of aeromagnetic data analysis (using 3D Euler deconvolution) in delineating active subsurface structures in the west central Arabian shield and the central Red Sea, Saudi Arabia: Arabian Journal of Geosciences, **7**, 4361-4376.

Alamdar, K., 2016. Interpretation of the magnetic data from Shavaz iron ore using enhanced local wavenumber (ELW) and comparison with Euler deconvolution method: Arabian Journal of Geosciences, **9**: 597. https://doi.org/10.1007/s12517-016-2616-2.

Alamdar, K., Kamkare-Rouhani, A., Ansari, A.H., 2015. Interpretation of the magnetic data from anomaly 2c of Soork iron ore using the combination of the Euler deconvolution and TDX filter: Arabian Journal of Geosciences, **8**, 6021-6035.

Alrafaee, H.A., 2017. Crustal modeling of the central part of Northern Western Desert, Egypt using gravity data: Journal of African Earth Sciences, **129**, 72-81.

Anand, S.P., Rajaram, M., Majumdar, T.J., Bhattacharyya, R., 2009. Structure and tectonics of 85°E Ridge from analysis of geopotential data: Tectonophysics, **478**, 100-110.

Araffa, S.A.S., Santos, F.A.M., Arafa-Hamed, T., 2012. Delineating active faults by using integrated geophysical data at northeastern part of Cairo, Egypt: NRIAG Journal of Astronomy and Geophysics, **1**, 33-34.

Araffa, S.A.S., Sabet, H.S., Gaweish, W.R., 2015. Integrated geophysical interpretation for delineating the structural elements and groundwater aquifers at central part of Sinai Peninsula, Egypt: Journal of South African Earth Sciences, **105**, 93-106.

Referências bibliográficas

Augusto, G.G.S.; Santos, E. J., 2014. São Raimundo Nonato - Folha SC.23-X- D-II: Estado do Piauí. Carta Geológica. Teresina: CPRM, mapa, color, 91,04 x 65,84 cm. Escala 1:100.000: Programa Geologia do Brasil - PGB. (available at <geosgb.cprm.gov.br>).

Awoyemi, M.O., Hammed, O.S., Falade, S.C., Arogundade, A.B., Ajama, O.D., Iwalehin, P.O., Olurin, O.T., 2017. Geophysical investigation of the possible extension of Ifewara fault zone beyond Ilesa area, southwestern Nigeria: Arabian Journal of Geosciences, **10**: 27. https://doi.org/10.1007/s12517-016-2813-z.

Bahrudin, N.F.D.B., Hamzah, U., 2018. Fault lineaments and depth estimation by aeromagnetic data of Mersing Fault Zone in Johore, Peninsular Malaysia: ARPN Journal of Engineering and Applied Sciences, **13**, 2108-2115.

Barbosa, V.C.F.; Silva, J.B.C e Medeiros, E. W., 1999. Stability analysis and improvement of structural index estimation in Euler deconvolution: Geophysics, **64**, 48-60.

Barbosa, V.C.F., Silva, J.B.C, Medeiros, E.W., 2000. Making Euler deconvolution applicable to small ground magnetic surveys: Journal of Applied Geophysics, **43**, 55-68.

Barbosa, V.C.F., Silva, J.B.C., 2005. Deconvolução de Euler: passado, presente e futuro - um tutorial: Revista Brasileira de Geofísica, **23**, 243-250.

Beiki, M., 2013. TSVD analysis of Euler deconvolution to improve estimating magnetic source parameters: An example from the Åsele area, Sweden: Journal of Applied Geophysics, **90**, 82-91.

Bizzi L.A., Schobbenhaus C., Vidotti R.M., Gonçalves & J.H. (orgs.). 2003. Geologia, tectônica e recursos minerais do Brasil: texto, mapas & SIG. CPRM - Serviço Geológico do Brasil, Brasília, 692 p.

Blakely, J.R., 1996. Potential Theory in Gravity and Magnetic Applications Cambridge University Press. Second Edition, p. 461.

Bournas, N., Galdeano, A., Hamoudi, M., Baker, H., 2003. Interpretation of the aeromagnetic map of Eastern Hoggar (Algeria) using the Euler deconvolution, analytic signal and local wavenumber methods: Journal of African Earth Sciences, **37**, 191-205.

Referências bibliográficas

Castro, D.L., 2011. Gravity and magnetic joint modeling of the Potiguar Rift Basin (NE Brazil): Basement control during Neocomian extension and deformation: Journal of South American Earth Sciences, **31**, 186-198.

Castro, D. L., Fuck, R. A., Philips, J. D., Vidotti, R. M., Bezerra, F. H. R., Dantas, E. L., 2014. Crustal structure beneath the Paleozoic Parnaíba Basin revealed by airborne gravity and magnetic data, Brazil: Tectonophysics, **614**, 128-145.

Castro, D.L., Fuck, R.A., Philips, J.D., Vidotti, R.M., Bezerra, F.H.R., Dantas, E.L., 2014. Crustal structure beneath the Paleozoic Parnaíba Basin revealed by airborne gravity and magnetic data, Brazil: Tectonophysics, 614, 128-145.

Chandrasekhar, E., Fontes, S.L., Flexor, J.M., Rajaram, M., Anand, S.P., 2009. Magnetotelluric and aeromagnetic investigations for assessment of groundwater resources in Parnaiba basin in Piaui State of North-East Brazil: Journal of Applied Geophysics, **68**, 269-281.

Chen, Q., Dong, Y., Cheng, S., Han, L., Xu, H., Chen, H., 2014. Interpretation of fault system in the Tana Sag, Kenya, using edge recognition techniques and Euler deconvolution: Journal of Applied Geophysics, **109**, 150-161.

Cooper, G.R.J., 2004. Euler Deconvolution applied to potential field gradients: Exploration Geophysics, **35**, 165-170.

Cooper, S.M., Liu, T., 2011. A magnetic and gravity investigation of the Liberia Basin, West Africa: Journal of South African Earth Sciences, **59**, 159-167.

Cordani, R., 2013. Constraint modelling in iron ore exploration. 13th International Congress of the Brazilian Geophysical Society & EXPOGEF, SBGF, 702-704. https://doi.org/10.1190/sbgf2013-145.

Cordani, R.; Shukowsky, W., 2009. Magnetização Remanente: Um parâmetro crucial para interpretação e Modelamento de Anomalias Magnéticas em território Brasileiro: Revista Brasileira de Geofísica, **27**, 659-667.

Curto, J.B., Vidotti, R.M., Blakely, R.J., Fuck, R.A., 2015. Crustal framework of the northwest Paraná Basin, Brazil: Insights from joint modeling of magnetic and gravity data: Tectonophysics, **655**, 58-72.

Dhaoui, M., Gabtni, H., Jallouli, C., Jleilia, A., Mickus, K.L., Turki, M.M., 2014. Gravity analysis of the Precambrian basement topography associated with the northern boundary of Ghadames Basin (southern Tunisia): Journal of Applied Geophysics, **111**, 299-311.

Referências bibliográficas

Ebbing, J., Skilbrei, J.R., Olesen, O., 2007. Insights into the magmatic architecture of the Oslo Graben by petrophysically constrained analysis of the gravity and magnetic field: Journal of Geophysical of Research, **112**, B04404. https://doi:10.1029/2006JB004694.

El Gout, R., Khattach, D., Houari, Mohammed-Rachid, Kaufmann, O., Aqil, H., 2010. Main structural lineaments of north-eastern Morocco derived from gravity and aeromagnetic data: Journal of South African Earth Sciences, **58**, 255-271.

Fairhead, J.D., Bennett, K.J., Gordon, D.R.H., Huang, D., 1994. Euler: Beyond the "Black Box". SEG Technical Program Expanded Abstracts, 422-424. https://doi.org/10.1190/1.1932113.

Fedi, M., Florio, G. 2013. Determination of the maximum-depth to potential field sources by a maximum structural index method: Journal of Applied Geophysics, **88**, 154-160.

Ferraccioli, F., Armadillo, E., Jordan, T., Bozzo, E., Corr, H., 2009. Aeromagnetic exploration over the East Antarctic Ice Sheet: A new view of the Wilkes Subglacial Basin: Tectonophysics, **478**, 62-77.

Ferraccioli, F., Bozzo, E., Damaske, D., 2002. Aeromagnetic signatures over western Marie Byrd Land provide insight into magmatic arc basement, mafic magmatism and structure of the Eastern Ross Sea Rift flank: Tectonophysics, **347**, 139-165.

Fitzgerald, D.; Reid, A. e Mclnerney, P., 2004. New discrimination techniques for Euler deconvolution: Computers & Geosciences, **30**, 461-469.

Geosoft 2015. Defining and applying filters and inverse FFT in MAGMAP. Geosoft Inc., 25p. <available at http://updates.geosoft.com/downloads/files/how-to-guides>

Gohl, K., Denk, A., Eagles, G., Wobbe, F., 2013. Deciphering tectonic phases of the Amundsen Sea Embayment shelf, West Antarctica, from a magnetic anomaly grid: Tectonophysics, **585**, 113-123.

Guoqing M., 2014. The application of extended Euler deconvolution method in the interpretation of potential field data: Journal of Applied Geophysics, **107**, 188-194.

Hadhemi, B., Fatma, H., Ali, K., Mohamed, G., 2016. Subsurface structure of Teboursouk and El Krib plains (dome zone, northern Tunisia) by gravity analysis: Journal of South African Earth Sciences, **119**, 78-93.

Referências bibliográficas

Harrouchi, L., Hamoudi, M., Bendaoud, A., Beguiret, L., 2016. Application of 3D Euler deconvolution and improved tilt angle to the aeromagnetic data of In Ouzzal terrane, western Hoggar, Algeria: Arabian Journal of Geosciences, **9**: 508. https://doi.org/10.1007/s12517-016-2536-1.

Hartman, R.R., Teskey, D.J., Friedberg, J.L., 1971. A system for rapid digital aeromagnetic interpretation: Geophysics, **36**, 891-918.

Hsu, S., 2000. Imaging magnetic sources using Euler's equation: Geophysical Prospecting, **50**, 15-25.

Ibraheem, I.M., Elawadi, E.A., El-Qady, G.M., 2018. Structural interpretation of aeromagnetic data for the Wadi El Natrun area, northwestern desert, Egypt: Journal of South African Earth Sciences, **139**, 14-25.

Kearey, P., Brooks, M., Hill, I., 2002. An introduction to geophysical exploration. Blackwell sciences. Third edition, p.281.

Khalil, M.H., 2016. Subsurface faults detection based on magnetic anomalies investigation: A field example at Taba protectorate, South Sinai: Journal of Applied Geophysics, **131**, 123-132.

Martins-Ferreira, M.A.C., Campos, J.E.G., Huelsen, M.G.V., Neri, B.L., 2018. Paleorift structure constrained by gravity and stratigraphic data: The Statherian Araí rift case: Tectonophysics, **738-739**, 64-82.

Mazabraud, Y., Béthoux, N., Deroussi, S., 2005. Characterisation of the seismological pattern in a slowly deforming intraplate region: central and western France: Tectonophysics, **409**, 175-192.

Melo, F.F., Barbosa, V.C.F., 2017. Correct structural index defined by base level estimates in Euler Deconvolution: 15th International Congress of the Brazilian Geophysical Society & EXPOGEF, SBGF, 1086-1091. https://doi.org/10.1190/sbgf2017-212.

Melo, F.F., Barbosa, V.C.F., 2017. What to expect from Euler Deconvolution estimates for isolated sources: 15th International Congress of the Brazilian Geophysical Society & EXPOGEF, SBGF, 1092-1097. https://doi.org/10.1190/sbgf2017-213.

Melo, F.F.; Barbosa, V.C.F.; Uieda, L.; Oliveira Jr., V.; Silva, J.B.C., 2013. Estimating the nature and the horizontal and vertical positions of 3D magnetic sources using Euler deconvolution: Geophysics **78**, 87-98.

Referências bibliográficas

Mieth, M., Jokat, W., 2014. Banded iron formation (?) at Grunehogna Craton, East Antarctica-constraints from aeromagnetic data: Precambrian Research, **250**, 143-150.

Mikhalov, V., Galdeano, A., Diament, M, Gvishiani, A., Agayan, S., Bogoutdinov, S., Graeva, E. e Sailhac, P., 2003. Application of artificial intelligence for Euler solutions clustering: Geophysics **68**, 168–180.

Minelli, L., Vecchio, A., Speranza, F., Nicolosi, I., Caracciolo, F.A., Chiappini, S., Carluccio, R., Chiappini, M., 2016. Aeromagnetic investigation of southern Calabria and the Messina Straits (Italy): Tracking seismogenic sources of 1783 and 1908 earthquakes: Journal of Geophysical of Research, **121**, 1297-1315.

Moghtaderi, N., Dehkordi, B.H., Oskooi, B., 2017. Characterization of the Houze-Vali iron ore in the centre of Iran using magnetic gradient tensor data: Bollettino di Geofisica Teorica ed Applicata, **58**, 205-216, doi: 10.4430/bgta0196.

Mushayandebvu MF; Van Driel P; Reid AB & Fairhead JD., 2001. Magnetic source parameters of two-dimensional structures using extended Euler deconvolution: Geophysics, **66**, 814-823.

Mushayandebvu MF; Lesur, V.; Reid AB & Fairhead JD., 2004. Grid Euler deconvolution with constraints for 2D structures: Geophysics, **69**, 489-496.

Naudy, H., 1971. Automatic determination of depth on aeromagnetic profiles. Geophysics, **36**, 717-722.

Ndougsa-Mbarga, T., Feumoe, A.N.S., Manguelle-Dicoum, E., Fairhead, J.D., 2012. Aeromagnetic Data Interpretation to Locate Buried Faults in South- East Cameroon: Geophysica, **48**, 49-63.

O'brien, D.P., 1972. CompuDepth – a new method for depth-to-basement calculation. In 42nd Annual International Meeting, Society of Exploration Geophysicists, Anaheim, California.

Okabe, M., 1979. Analytical expressions for gravity anomalies due to homogeneous polyhedral bodies and translations into magnetic anomalies: Geophysics, **44**:730-741.

Oladunjoye, M.A., Olayinka, A.I., Alaba, M.; Adabanija, M.A., 2016. Interpretation of high resolution aeromagnetic data for lineaments study and occurrence of banded iron formation in Ogbomoso area, Southwestern Nigeria: Journal of African Earth Sciences, **114**, 43-56.

Referências bibliográficas

Olasunkanmi, N.K., Bamigboye, O.S., Aina, A., 2017. Exploration for iron ore in Agbado-Okudu, Kogi State, Nigeria: Arabian Journal of Geosciences, **10**:541. https://doi.org/10.1007/s12517-017-3250-3.

Oruç, B., Keskinsezer, A., 2008. Detection of causative bodies by normalized full gradient of aeromagnetic anomalies from east Marmara region, NW Turkey: Journal of Applied Geophysics, **65**, 39-49.

Oruç, B., Selim, B.B., 2011. Interpretation of magnetic data in the Sinop area of Mid Black Sea, Turkey, using tilt derivative, Euler deconvolution, and discrete wavelet transform: Journal of Applied Geophysics, **74**, 194-204.

Osinowo, O.O., Akanji, A.O., Olayinka, A.I., 2014. Application of high resolution aeromagnetic data for basement topography mapping of Siluko and environs, southwestern Nigeria: Journal of South African Earth Sciences, **99**, 637-651.

Reeh, G., Aifa, T., 2008. Age of the source of the Jarrafa gravity and magnetic anomalies offshore Libya and its geodynamic implications: Journal of Geodynamics, **45**, 217-233.

Reid, A.B., 2003. Euler magnetic structural index of a thin-bed fault: Geophysics, **68**, 1255-1256.

Reid, A.B.; Allsop, J.M. Granser; H., Millettg, A.J. e Somerton, I.W., 1990. Magnetic interpretation in three dimensions using Euler deconvolution. Geophysics, **55**, 80-91.

Rocha, L.G.M., Pires, A.C.B., Carmelo, A.C., Filho, J.O.A., 2014. Geophysical characterization of the azimuth 125° lineament with aeromagnetic data: Contributions to the geology of central Brazil: Precambrian Research, **249**, 273-287.

Rodrigues, R.S.; Castro, D.L.; JÚNIOR, J.A. R., 2014. Characterization of the Potiguar Rift Structure Based on Euler Deconvolution: Brazilian Journal of Geophysics, **32**, 109-121.

Silva, B.C.J., 1986. Reduction to the pole as an inverse problem and its application to low latitude anomalies: Geophysics, **51**, 369-382.

Silva, J.B.C.; Barbosa, V.C.F. & Medeiros, W.E., 2001. Scattering, symmetry, and bias analysis of source-position estimates in Euler deconvolution and its practical implications: Geophysics, **66**, 1149-1156.

Sridhar, M., Babu, V.R., Markandeyulu, A., Raju, B.V.S.N., Chaturvedi, A.K., Roy, M.K., 2017. A reassessment of the archean-mesoproterozoic tectonic development of the southeastern Chhattisgarh Basin, Central India through detailed aeromagnetic analysis: Tectonophysics, **712-713**, 289-302.

Referências bibliográficas

Thompson, D.T., 1982. EULDPH: A new technique for making depth estimates from magnetic data: Geophysics, **47**, 31-37.

Uchôa Filho, E.A., Freitas, M.S., 2017. Complexos Santa Filomena e Paulistana. Teresina, CPRM. Mapa colorido 163,99 x 89,99 cm. Escala 1:100.000. Integração geológica e de recursos minerais das faixas marginais da borda norte-noroeste do Cráton São Francisco (Empreendimento Áreas de Relevante Interesse Mineral-ARIM). (available at <geosgb.cprm.gov.br>).

Ugalde, H. e Morris, W. A., 2010. Cluster analysis of Euler deconvolution solutions: New filtering techniques and geologic strike determination: Geophysics, **75**, 61-70.

Uieda, L., Oliveira, J.R, V.C., Barbosa, V.C.F., 2014. Geophysical tutorial: Euler deconvolution of potential-field data: The Leading Edge, **33**, 448-450.

Wang, J., Meng, X., Li, F., 2017. New improvements for lineaments study of gravity data with improved Euler inversion and phase congruency of the field data: Journal of Applied Geophysics, **136**, 326-334.

Weihermann, J.D., Ferreira, F.J.F., Oliveira, S.P., Cury, L.F., Souza, J., 2018. Magnetic interpretation of the Paranaguá Terrane, southern Brazil by signum transform: Journal of Applied Geophysics, **154**, 116-127.

Werner, S.C., Torsvik, T.H., 2010. Downsizing the Mjølnir impact structure, Barents Sea, Norway: Tectonophysics, **483**, 191-202.

Zhang, J., Zhao, G., Shen, W., Li, S., Sun, M., 2015. Aeromagnetic study of the Hengshan-Wutai-Fuping region: Unraveling a crustal profile of the Paleoproterozoic Trans-North China Orogen: Tectonophysics, **662**, 208-218.

APÊNDICE

Modelagem Magnética Direta 3D

As modelagens sintéticas do estudo foram baseadas na proposta de Okabe (1979). O autor utilizou a Relação de Poisson e a Terceira Identidade de Green correlacionada com o princípio da superposição para obter o campo magnético de corpos poliédricos compostos por facetas poligonais.

O potencial magnético é obtido a partir da primeira derivada do potencial gravitacional em uma dada direção e o campo magnético em uma direção arbitrária é adquirido a partir da segunda derivada do potencial gravitacional pela Relação de Poisson. A seguir, será descrito de forma breve os passos seguidos pelo autor para obter o campo magnético de corpos poliédricos.

Regras de Transformação do Campo Gravimétrico em Magnético

Dado o potencial gravitacional U na origem P devido a um corpo de volume V:

$$U = -G\int_{v} \rho u \ dV \ , \qquad\qquad \text{Eq. (3.1)}$$

onde G é a constante de gravitação universal, ρ é a densidade do corpo e $u = -(x^2 + y^2 + z^2)^{-\frac{1}{2}}$ à distância do corpo ao ponto de observação. A primeira derivada do potencial gravitacional na direção **k** é dada por:

$$U_k = -\nabla(U) \cdot \boldsymbol{k} \ , \qquad\qquad \text{Eq. (3.2)}$$

onde ∇ é o operador gradiente (∂/∂x, ∂/∂y, ∂/∂z), e $\boldsymbol{k}$ é o vetor direção na k-ésima direção,

$$\boldsymbol{k}^t = (k_x, k_y, k_z)$$
$$ou \qquad\qquad \text{Eq. (3.3)}$$
$$\boldsymbol{k}^t = [\cos(x,k), \cos(y,k), \cos(z,k)]$$

sendo cos(x,k), o cosseno direcional da k-ésima direção na direção $\boldsymbol{x}$ e assim por diante. Substituindo a Equação (2.1) em (2.2), tem-se:

$$U_k = G\int_{V} \nabla(\rho u) \cdot \boldsymbol{k} \ dv \qquad\qquad \text{Eq. (3.4)}$$

E aplicando o teorema da divergência:

$$U_k = G \int_S \rho u \cdot \boldsymbol{k}^t \boldsymbol{n} \ dS \ ,$$ Eq.(3.5)

sendo S a superfície do corpo de volume V e $\boldsymbol{n}$ a direção do vetor especificando a normal pra fora da superfície infinitesimal dS.

Adicionando a direção l, a segunda derivada do potencial gravitacional U_{kl} pode ser obtida:

$$U_{kl} = -G \int_V \nabla \cdot \left[\nabla(\rho u) \cdot \boldsymbol{k} \right] \boldsymbol{l} \ dV$$ Eq.(3.6)

O teorema da divergência torna a equação (2.6) como:

$$U_{kl} = -G \int_S \boldsymbol{l}^t \boldsymbol{n} \cdot \nabla(\rho u) \cdot \boldsymbol{k} \ dS$$ Eq.(3.7)

Okabe (1979) utiliza a relação de Poisson para obter o campo magnético de poliedros. O autor transforma a expressão do potencial gravimétrico demonstrado na equação (3.5) em potencial magnético fazendo $G\rho = 1$ e considerando $\boldsymbol{k}$ como vetor de intensidade magnética. Além disso, considera o campo magnético do corpo na direção $\boldsymbol{k}$ obtido a partir da derivação do potencial gravimétrico (equação 3.7), sendo l o vetor de intensidade magnética.

Admite-se que o corpo poliédrico é composto de várias facetas poligonais. Portanto, empregando o princípio da superposição, o campo magnético do corpo será obtido pelo somatório da contribuição magnética individual de cada faceta que compõe o corpo. O algoritmo de modelagem utilizado é flexível quanto à forma geométrica do corpo a ser modelado, e permite adicionar vértices ao corpo para compor o modelo.

Etapas da modelagem

A modelagem é composta por duas fases:

1ª Etapa - gerar o prisma associado à fonte anômala. Os parâmetros de entrada do prisma são: a) dimensões (altura, largura e profundidade); b) profundidade do topo do prisma; c) magnetização do prisma em A/m; d) declinação e inclinação; e) parâmetros do

grid de amostragem (n° de pontos nas direções norte e leste; espaçamento da amostragem, coordenadas iniciais); f) desvio padrão do ruído a ser inserido no campo observado; g) direção (declinação e inclinação) do campo observado; h) posição do corpo no grid e i) ângulos de rotação do prisma.

2ª Etapa – calcular o campo magnético de cada face do prisma gerado. A figura 5 apresenta alguns exemplos da composição de corpos anômalos possíveis neste tipo de modelagem.
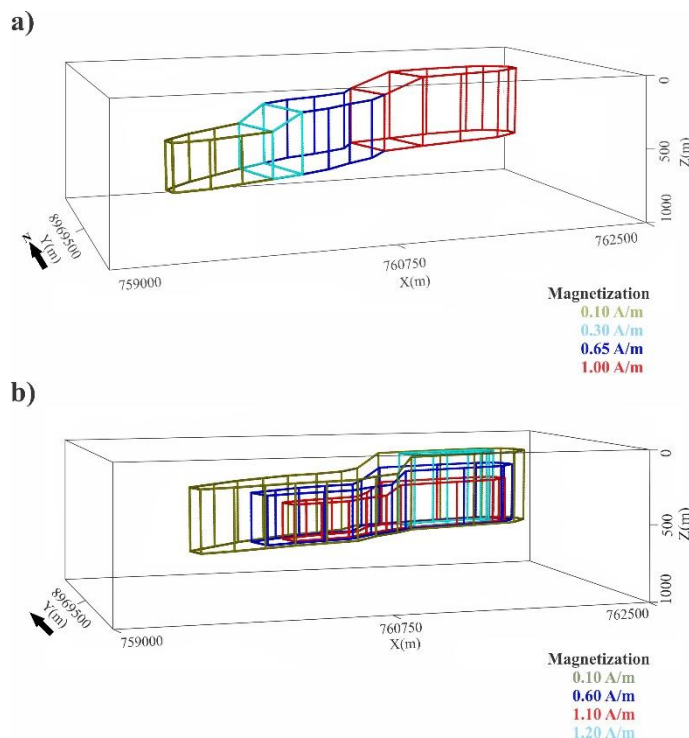

Figura 5: Exemplos de composição de corpos anômalos a partir de Okabe 1979. Em a), corpo com contraste de magnetização lateral e b) corpo com contraste interno de magnetização.